Article

Journal of Vibration and Control
2021, Vol. 27(1–2) 82–100

DOI: 10.1177/1077546320923933
journals.sagepub.com/home/jvc
SAGE

Numerical verification of variable friction cladding connection for multihazard mitigation

Yongqiang Gong[1], Liang Cao[2], Simon Laflamme[1,3], James Ricles[2,4], Spencer Quiel[2,4] and Douglas Taylor[5]

Abstract

The motion of cladding systems can be leveraged to mitigate natural and man-made hazards. The literature counts various examples of connections enhanced with passive energy dissipation capabilities at connections. However, because such devices are passive, their mitigation performance is typically limited to specific excitations. The authors have recently proposed a novel variable friction cladding connection capable of mitigating hazards semi-actively. The variable friction cladding connection is engineered to transfer lateral forces from the cladding element to the structural system. Its variation in friction force is generated by a toggle-actuated variable normal force applied onto sliding friction plates. In this study, a multiobjective motion-based design methodology integrating results from the previous work is proposed to leverage the variable friction cladding connection for nonsimultaneous wind, seismic, and blast hazard mitigation. The procedure starts with the quantification of each hazard and performance objectives. It is followed by the selection of dynamic parameters enabling prescribed performance under wind and seismic loads, after which an impact rubber bumper is designed to satisfy motion requirements under blast. Last, the peak building responses are computed and iterations conducted on the design parameters on the satisfaction of the motion objectives. The motion-based design procedure is verified through numerical simulations on two example buildings subjected to the three nonsimultaneous hazards. The performance of the variable friction cladding connection is also assessed and compared against different control cases. Results show that the motion-based design procedure yields a conservative design approach in meeting all of the motion requirements and that the variable friction cladding connection performs significantly well at mitigating vibrations.

Keywords

Motion-based design, cladding, multiple hazards, semiactive control, variable friction, high performance control system

1. Introduction

Motion-based design (MBD) is a design strategy that consists of sizing a structural system to meet a given level of motion criteria under design loads (Connor and Laflamme, 2014). This strategy may include the incorporation of supplemental damping systems during the structure's design, construction, and rehabilitation phases (Filiatrault et al., 2001; Guo and Christopoulos, 2013). Over the last decades, passive energy dissipation systems have been widely accepted and deployed to enhance structural resiliency against natural and man-made hazards. Because the performance of these systems is typically frequency bandwidth–limited, they are usually designed and used to mitigate a single type of hazards. A solution to improve structural performance to multiple types of hazards, or multihazards, is the design of semi-active (Bitaraf et al., 2010; Cao et al., 2018a) or hybrid (Fisco and Adeli, 2011; Kim and Kang, 2011) energy dissipation systems, which have been shown capable of high mitigation performance over large frequency bandwidths using limited power input

[1]Department of Civil, Construction, and Environmental Engineering, Iowa State University, USA
[2]ATLSS Engineering Research Center, Lehigh University, USA
[3]Department of Electrical and Computer Engineering, Iowa State University, USA
[4]Department of Civil and Environmental Engineering, Lehigh University, USA
[5]Taylor Devices, USA

Received: 5 July 2019; accepted: 2 April 2020

Corresponding author:
Liang Cao, ATLSS Engineering Research Center, Lehigh University, 117 ATLSS Drive, Room B214, Bethlehem 18015, PA, USA.
Email: lic418@lehigh.edu

(Cao et al., 2016). Of interest to this study are energy dissipation systems at the cladding level, in particular damping strategies addressing the multihazard mitigation challenge.

Early research on leveraging cladding for energy dissipation focused on blast mitigation using sacrificial cladding panels and energy dissipative cladding connections. Sandwich cladding (Alberdi et al., 2013; Yang et al., 2011), double-layer foam cladding (Ma and Ye, 2007; Wu and Sheikh, 2013), and composite tube-core cladding (Theobald and Nurick, 2010; Van Paepegem et al., 2014) are examples of sacrificial cladding elements, whereas rotational friction hinge (Chen and Hao, 2013a, 2013b), viscoelastic spider (Amadio and Bedon, 2012), and metallic yielding connections (Wang et al., 2017) are examples of blast mitigation connections. Passive cladding connections have also been proposed to reduce wind and seismic vibrations. For example hysteretic cladding connections including U-shaped flexural plate connectors (Baird et al., 2013) and W-shaped folded steel plate connectors (Dal Lago et al., 2018) have been presented and tested for seismic mitigation. Frictional cladding connections, including bolted friction connectors (Ferrara et al., 2011) and braced friction connectors (Maneetes and Memari, 2014), have been implemented to supplement the lateral load resistance for cladding. Advanced flexural cladding connections are also been studied to leverage the inertia of the cladding system in mitigating vibrations (Fu and Zhang, 2016; Pipitone et al., 2018).

Limited semi-active energy dissipation systems at the cladding level have been studied by the research community. The authors have recently proposed a variable friction cladding connection (VFCC) (Gong et al., 2018). The device leverages the inertia of cladding elements for multihazard mitigation. Other mitigation systems using the inertia of building components have been proposed in the literature (Anajafi and Medina, 2018b; Sakr, 2017; Xiang and Nishitani, 2014, 2015). Here, the VFCC is engineered to laterally connect cladding elements to the structural system. Its variable friction force is generated by sliding friction plates onto which a variable normal force is applied via an adjustable toggle system. The characterization of the VFCC's friction mechanism has been conducted in a laboratory environment on a prototype (Gong et al., 2018). The authors have also developed MBD procedures and numerically demonstrated the ability of the VFCC to improve building performance under three individual hazards: wind (Gong et al., 2019a), seismic (Gong et al., 2019b), and blast (Cao et al., 2018b). The objective of this paper is to integrate these results for multihazard mitigation by meeting multi-objective requirements.

The paper is organized as follows. The background on the VFCC device is presented in Section 2. Analytical transfer functions that are the foundations of MBD procedures under wind, seismic, and blast hazards are summarized in Section 3. The multihazard design procedure is introduced in Section 4. The MBD procedure on two prototype buildings is numerically verified in Section 5. The paper is summarized and concluded in Section 6.

2. Semi-active cladding connection

The VFCC device is shown in Figure 1. It consists of two sets of friction plates onto which a variable pressure is applied by an actuator via adjustable toggles. It is engineered to be used under different control states. During daily operation, the VFCC is locked to provide a high friction force by keeping the toggles in a vertical alignment (Figure 1(a)). In this high friction state, there is no slippage under low-to-moderate loadings and the VFCC acts as a stiff connector. This locked state is passive and also used to mitigate blast, where the maximum static friction force is designed to be exceeded by the design blast load and to enable energy dissipation via slippage. Remark that semi-active control capabilities are not activated to mitigate a blast load because of the high rate nature of the event (Hong et al., 2018). For wind and seismic applications, the VFCC is used as a variable friction damper by actuating the

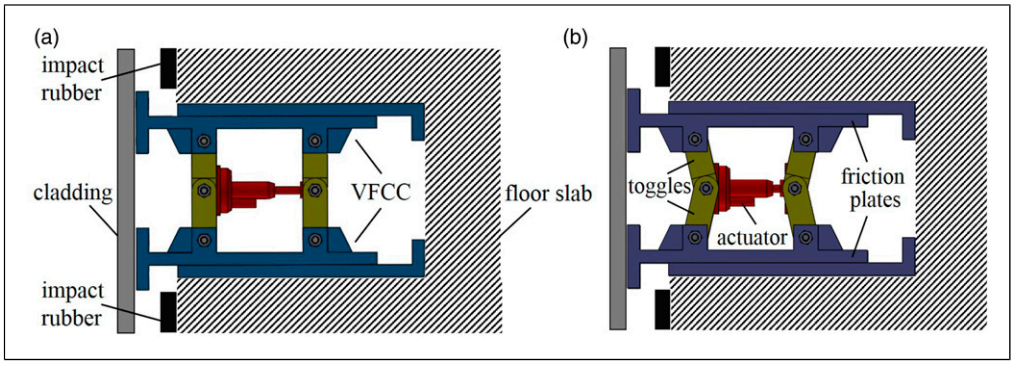

Figure 1. Variable friction cladding connection installed in a floor slab (top view) showing two control states: (a) locked device and (b) semi-locked device.

toggles (Figure 1(b)), where structure–cladding motions are leveraged to limit acceleration transfer and/or reduce interstory drift.

The dynamic characterization of the device was conducted on a fabricated prototype in a laboratory environment in the prior work (Gong et al., 2018). A LuGre friction model was used to represent its dynamic friction force F_f versus the sliding displacement x. Figure 2 shows representative dynamic response of the device prototype in terms of actuation capacity using the parameterized LuGre model.

2.1. Impact rubber model

A nonlinear impact model for rubber shock absorbers was selected to simulate the use of the rubber impact bumper with the VFCC. It consists of the 3-stage nonlinear hysteretic model developed by Polycarpou et al. (2013). The model was applied to mitigate blast effects in the prior work (Cao et al., 2018b). The impact force F_r is characterized by

$$F_r = \begin{cases} k_r x_r^{2.65} & \text{if} \quad x_r \le x_{r,u}\ \dot{x}_r > 0 \\ k_r x_{r,u}^{2.65} + k_{r,y}(x_r - x_{r,u}) & \text{if} \quad x_r > x_{r,u}\ \dot{x}_r > 0 \\ k_r x_r^{2.65}(1 + c_r \dot{x}_r) & \text{if} \quad \dot{x}_r < 0 \end{cases} \tag{1}$$

where x_r and $x_{r,u}$ are the indentation and the ultimate compression capacity of the rubber bumper, respectively, $\dot{x}_r$ represents the relative velocity of the colliding surfaces, k_r, and $k_{r,y}$ are the impact stiffness constant and the postyield stiffness, respectively, and c_r is the impact damping coefficient. The value of c_r is estimated using the semi-empirical equation from Polycarpou et al. (2013)

$$c_r = \frac{3\left(1 - c_{r0}^2\right)}{2 c_{r0} \dot{x}_{\text{imp}}} \tag{2}$$

where $\dot{x}_{\text{imp}}$ is the impact velocity and c_{r0} is the coefficient of restitution. The impact stiffness k_r of a specific rubber bumper is taken as

$$k_r = U_r k_{r,s} = U_r K_r A_r l_r^{-2.65} \tag{3}$$

where $U_r > 1$ is a strain rate–dependent coefficient and $k_{r,s}$ is the static stiffness of the rubber pad, which is computed based on the material's stiffness K_r, the contact area of the bumper A_r, and the bumper's thickness l_r. Example values for all parameters are given in Polycarpou et al. (2013).

3. Methodology

In this section, the analytical transfer functions characterizing the structure–cladding interaction under wind, seismic, and blast loads are presented. These transfer functions will be used for conducting the MBD process.

3.1. Structure–cladding model

The structure equipped with the semi-active cladding system is assumed to behave elastically following the MBD procedure. First, the structure is simplified into a lumped-mass shear building. Second, a cladding panel is simplified as a rigid mass spanning two adjacent floors and laterally connected to the structural system through the VFCC, assuming that the gravitational load is taken by a traditional connector. Figure 3(a) shows an n-story structure equipped with a semi-active cladding system, and Figure 3(b) shows the VFCC connection. The VFCC connection includes a stiffness element k_c, a viscous damping element c_{c0}, a variable friction element producing a constant friction force F_c under blast or an adjustable friction force F_f under seismic and wind loads, and a rubber bumper element producing a force F_r (equation (1)). Note that $x_{c,i}$ refers to the relative displacement between the ith cladding point to its connected structural floor.

3.1.1. Equations of motion under blast load. The equations of motion of the system under blast load are derived for

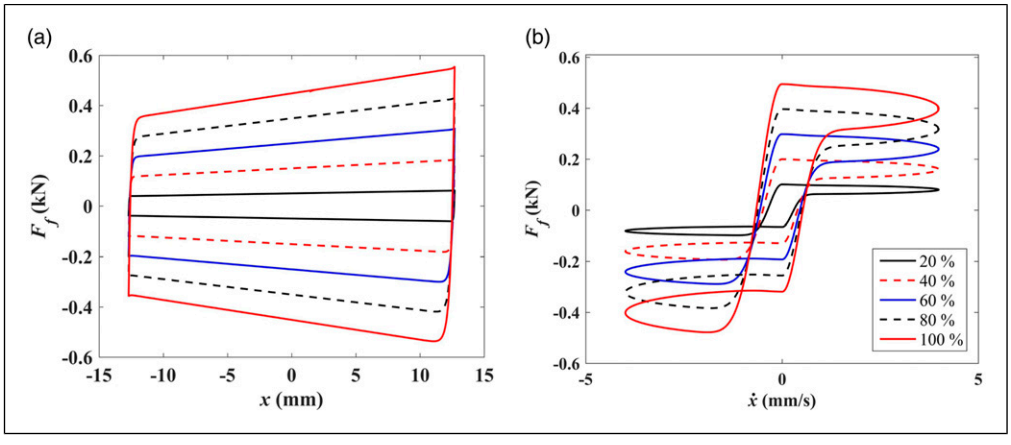

Figure 2. Dynamics of the friction device under a harmonic excitation of amplitude 13 mm at 0.05 Hz under various levels of actuation capacity: (a) force–displacement loop and (b) force–velocity loop.

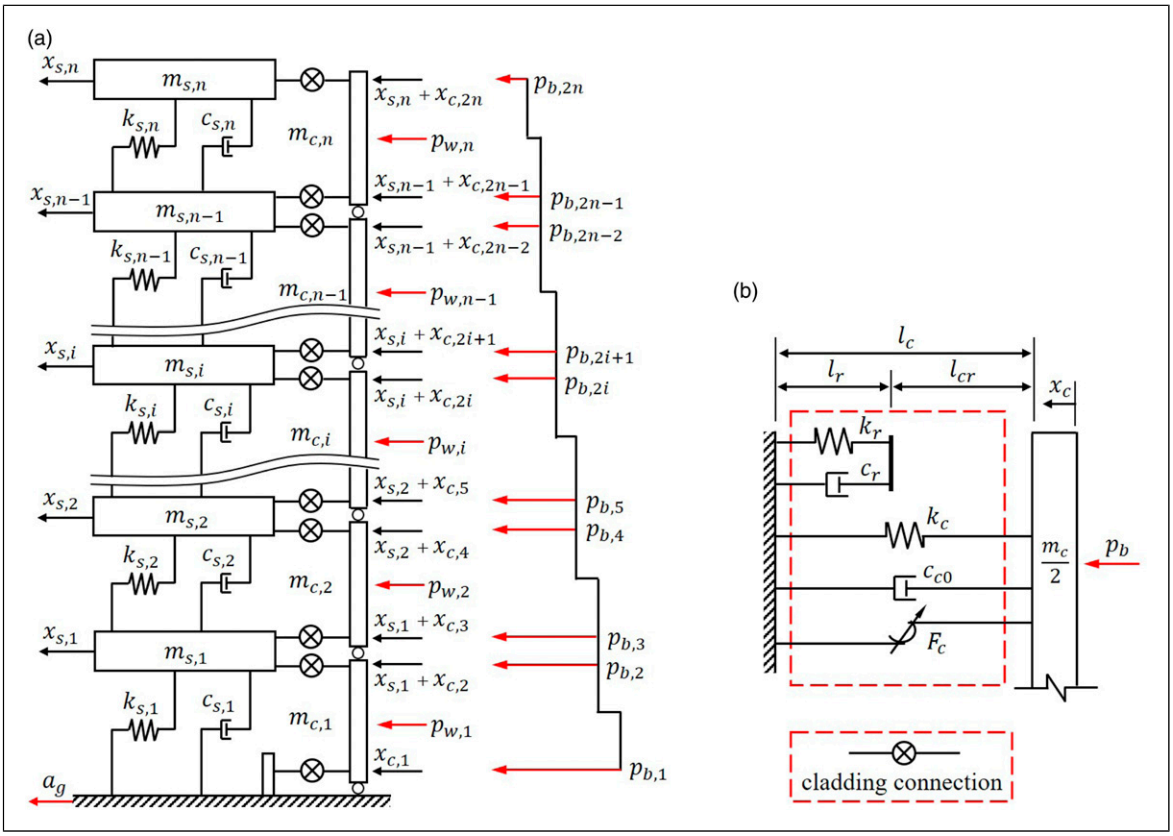

Figure 3. Simplified representations for an *n*-story structure equipped with a semi-active cladding system: (a) structure–cladding model and (b) cladding connection model.

a high-rate blast event. A typical air blast pressure wave where the high-rate air pressure rapidly builds up to a peak reflected pressure value σ_p and then decays over duration t_p (Li and Meng, 2002). The pressure continues to drop to the negative pressure σ_n and gradually dissipates over duration t_n (Larcher, 2008). This typical air blast pressure is approximated by an idealized model through linearizing its positive phase and neglecting the negative pressure region (i.e. $\sigma_n \approx 0$), yielding the associated blast load $p_b(t)$ (Cao et al., 2018b)

$$p_b(t) = \begin{cases} \hat{p}_b\left(1 - \dfrac{t}{t_p}\right) & \text{if} \quad 0 < t < t_p \\ 0 \quad \text{if} \quad t > t_p \end{cases} \tag{4}$$

where the peak value of blast load $\hat{p}_b = \sigma_p A$ and A is the area of the cladding element. The blast-induced forces are assumed to fully transfer to the structure through the cladding connections, with no blast energy dissipation or absorption from the cladding element, yielding a conservative solution (Cao et al., 2018b).

Considering the rapid time decay of the blast load, the structure–cladding interaction at each connecting node is studied using the single-degree-of-freedom (SDOF) model shown in Figure 3(b). In this configuration, the structural floor is assumed to be fixed assuming that the dynamic response of the primary structure itself is negligible during the first half-cycle of the cladding motion (Karagiozova et al., 2010; Olmati et al., 2014). The equations of motion of the SDOF representation are developed to compute the peak dynamic response of the cladding element

$$m_c\ddot{x}_c + c_{c0}\dot{x}_c + k_c x_c + F_c(\dot{x}_c) = \hat{p}_b\left(1 - \frac{t}{t_p}\right) \quad \text{for} \quad 0 < t < t_p \tag{5a}$$

$$m_c\ddot{x}_c + c_{c0}\dot{x}_c + k_c x_c + F_c(\dot{x}_c) = 0 \quad \text{for} \quad t_p \le t < t_r \tag{5b}$$

$$m_c\ddot{x}_c + c_{c0}\dot{x}_c + \left(k_c + k_{eq}\right)x_c + F_c(\dot{x}_c) = 0 \quad \text{for} \quad t \ge t_r \tag{5c}$$

with the friction force of the passive-on (ON) VFCC represented by the Coulomb model

$$F_c(\dot{x}_c) = \begin{cases} -F_{c0} & \text{if} \quad \dot{x}_c < 0 \\ 0 \quad \text{if} \quad \dot{x}_c = 0 \\ F_{c0} \quad \text{if} \quad \dot{x}_c > 0 \end{cases}$$

where t_r is the time point when the cladding hits the rubber surface. Remark that results from a previous study showed

that $t_r \gg t_p$ (Cao et al., 2018b). Once the cladding panel collides with the impact rubber bumper, the system dynamics is represented by equation (5c) and the rubber model is approximated using a linear stiffness element k_{eq} to obtain the analytical solution of the maximum rubber deformation. Note that the linear stiffness element cannot dissipate energy during a full cycle of harmonic motion. It is only used to represent the rubber dynamics during the gap-closing phase. To do so, the hysteresis of the impact rubber bumper is compared with that of a linear stiffness element over the first quarter cycle of harmonic motion. Assuming a periodic motion of the impact rubber surface $x_r(t) = \bar{x}_r \sin(\Omega t)$, the energy dissipation of the equivalent stiffness element W_r over this quarter cycle is expressed as

$$W_r = \int_0^{\bar{x}_r} k_{eq} x_r dx_r = \frac{1}{2} k_{eq} \bar{x}_r^2 \tag{6}$$

where $\bar{x}_r$ is the amplitude of periodic motion and assumed to be half the thickness of impact rubber to avoid exceeding the ultimate compression capacity $x_{r,u} = 80\%\ l_r$ reported in Polycarpou et al. (2013). The energy dissipation W_r at the approaching phase of the rubber bumper can be computed using equation (1)

$$W_r = \int_0^{\bar{x}_r} F_r dx_r = \int_0^{\bar{x}_r} k_r x_r^{2.65} dx_r = \frac{1}{3.65} k_r \bar{x}_r^{3.65} \tag{7}$$

and equating equations (6) and (7) gives $k_{eq} = 0.55 k_r \bar{x}_r^{1.65}$.

3.1.2. Equations of motion under wind and seismic loads. Under wind and seismic loads, the structure–cladding spacing l_c and rubber thickness l_r are designed such that $l_{cr} = l_c - l_r > x_c$ (Figure 3(b)) to prevent the cladding element from colliding with the rubber bumper. For simplicity of the design process and field applications, the mass of cladding panel m_c, stiffness k_c,, and viscous damping c_c of the cladding connection are taken to be identical at each floor. Following the assumptions of equivalent viscous damping and approximating motion through the first modal response of the structure and the cladding (as verified in Gong et al. (2019a, 2019b)), the governing equations of the structure–cladding system under loads of $p_{w,i}$, and a_g are reduced to

$$\begin{aligned} &m_{se}\ddot{q}_{s1} + c_{se}\dot{q}_{s1} + k_{se}q_{s1} \\ &\quad = -\sum_{i=1}^{n} \phi_{s,1i} m_{si} a_g + \sum_{i=1}^{n} \alpha_i \left(k_{ce} q_{c1,i} + c_{ce}\dot{q}_{c1,i}\right) \end{aligned} \tag{8}$$

$$m_{ce}\ddot{q}_{c1,i} + c_{ce}\dot{q}_{c1,i} + k_{ce}q_{c1,i} = p_{w,i} - m_{ce}a_g - \alpha_i m_{ce}\ddot{q}_{s1} \tag{9}$$

where $\Phi_{s1} = \begin{bmatrix} \phi_{s,11} & \phi_{s,12} & \cdots & \phi_{s,1n} \end{bmatrix}^T$ is the first modal vector of the primary structure with $\phi_{s,1n}$ normalized to unity, and $\alpha_i = (1/2)(\phi_{s,1i-1} + \phi_{s,1i})$ for $i = 2, \ldots, n$ and $\alpha_i = (1/2)\phi_{s,1i}$ for $i = 1$ are the nodal displacements of the equivalent SDOF structure $q_{s1} \approx x_{sn}$ of dynamic properties defined as

$$m_{se} = \Phi_{s1}^T \mathbf{M}_s \Phi_{s1};\quad c_{se} = \Phi_{s1}^{\mathrm{T}} \mathbf{C}_s \Phi_{s1};\quad k_{se} = \Phi_{s1}^{\mathrm{T}} \mathbf{K}_s \Phi_{s1} \tag{10}$$

where $\mathbf{M}_s \in \mathbb{R}^{n\times n}$, $\mathbf{C}_s \in \mathbb{R}^{n\times n}$, and $\mathbf{K}_s \in \mathbb{R}^{n\times n}$ are, respectively, the mass, damping, and stiffness matrices associated with the primary structure.

The first modal vector of each cladding element $\Phi_{c1} = [1\ \ 1]^T$ and the nodal displacement of the ith cladding element $q_{c1,i} \approx x_{c,2i-1} \approx x_{c,2i}$ are used to construct an expression for the cladding modal mass m_{ce}, damping c_{ce}, and stiffness k_{ce}

$$\begin{aligned} &m_{ce} = \Phi_{c1}^T \mathbf{m}_c \Phi_{c1} = m_c;\quad c_{ce} = \Phi_{c1}^T \mathbf{c}_c \Phi_{c1} = 2c_c; \\ &k_{ce} = \Phi_{c1}^T \mathbf{k}_c \Phi_{c1} = 2k_c \end{aligned}$$

where $\mathbf{m}_c \in \mathbb{R}^{2\times2}$, $\mathbf{c}_c \in \mathbb{R}^{2\times2}$, and $\mathbf{k}_c \in \mathbb{R}^{2\times2}$ are, respectively, the mass, damping, and stiffness matrices associated with each cladding element.

3.2. Transfer functions

3.2.1. Blast load. The transfer solutions of blast-induced response (equation (5)) are derived using Duhamel's integral, and the analytical solutions after integration by parts when $0 < t < t_p$ are given by (Cao et al., 2018b)

$$\begin{aligned} x_c(t) = e^{-\xi\omega_n t}&\left[\left(x_0 - \frac{F_c}{k_c}\right)\cos\omega_d t \right. \\ &\left. + \frac{\dot{x}_0 + (x_0 - (F_c/k_c))\xi\omega_n}{\omega_d}\sin\omega_d t\right] + \frac{F_c}{k_c} \\ &+ \frac{\hat{p}_b}{k_c}\left[1 - e^{-\xi\omega_n t}\left(\frac{\xi}{\sqrt{1-\xi^2}}\sin\omega_d t + \cos\omega_d t\right)\right] \\ &- \frac{\hat{p}_b}{k_c t_p}\left[t - \frac{2\xi}{\omega_n} + \frac{e^{-\xi\omega_n t}}{\omega_n}\left(2\xi\cos\omega_d t \right.\right. \\ &\left.\left. + \frac{2\xi^2 - 1}{\sqrt{1-\xi^2}}\sin\omega_d t\right)\right] \end{aligned} \tag{11}$$

and

$$\begin{aligned} \dot{x}_c(t) = e^{-\xi\omega_n t}&\left[\dot{x}_0\cos\omega_d t \right. \\ &\left. - \left(\frac{x_0\omega_n - (F_c/k_c)\omega_n + \xi\dot{x}_0}{\sqrt{1-\xi^2}}\right)\sin\omega_d t\right] \\ &+ \frac{\hat{p}_b\omega_n e^{-\xi\omega_n t}}{k_c\sqrt{1-\xi^2}}\sin\omega_d t - \frac{\hat{p}_b}{k_c t_p}\left[1 - e^{-\xi\omega_n t}\left(\cos\omega_d t \right.\right. \\ &\left.\left. + \frac{\xi}{\sqrt{1-\xi^2}}\sin\omega_d t\right)\right] \end{aligned} \tag{12}$$

where x_0 and $\dot{x}_0$ are the initial conditions at $t = 0$ and ξ, ω_n, and ω_d are the damping ratio, natural frequency, and damped frequency of the cladding element, respectively. Note that the above solution is derived for each connection node and the corresponding cladding mass for blast design m_b is taken as half of the cladding mass m_c (e.g. $m_b = m_c/2$). The solutions of equations (11) and (12) with $x_c(t_p)$ and $\dot{x}_c(t_p)$ at $t = t_p$ are then used as initial conditions to solve equation (5b), yielding

$$x_c(t) = e^{-\xi\omega_n(t-t_p)}\left[\left(x_c(t_p) - \frac{F_c}{k_c}\right)\cos\omega_d(t-t_p) + \frac{\dot{x}_c(t_p) + \left(x_c(t_p) - (F_c/k_c)\right)\xi\omega_n}{\omega_d}\sin\omega_d(t-t_p)\right] + \frac{F_c}{k_c} \tag{13}$$

where $t_p \le t < t_r$. Taking the derivative of equation (13) equal to zero, the maximum displacement of the cladding $x_{c,\max}$ without considering the rubber bumper element is expressed

$$x_{c,\max} = e^{-\xi\omega_n(t_1-t_p)}\frac{\sqrt{\left[x_c(t_p) - (F_c/k_c)\right]^2\omega_d^2 + \left[\dot{x}_c(t_p) + \left(x_c(t_p) - (F_c/k_c)\right)\xi\omega_n\right]^2}}{\omega_d} + \frac{F_c}{k_c} \tag{14}$$

with the occurring time t_1 in the first cycle

$$t_1 = \omega_d^{-1}\tan^{-1}\left[\frac{\dot{x}_c(t_p)\sqrt{1-\xi^2}}{\left(x_c(t_p) - (F_c/k_c)\right)\omega_n + \xi\dot{x}_c(t_p)}\right] + t_p \tag{15}$$

Note that $x_{c,\max}$ refers to the maximum absolute value of all structure–cladding displacement $x_{c,i}$ ($x_{c,\max} = \max(|x_{c,1}(t)|, |x_{c,2}(t)|, \cdots, |x_{c,2n}(t)|)$). Following the collision time t_r, if occurs, the rubber deformation $x_r(t)$ is obtained by solving equation (5c), which is similar to the solutions for equation (5b) but with a new stiffness element $k_{\text{new}} = k_c + k_{eq}$. The maximum rubber deformation $x_{r,\max}$ is derived

$$x_{r,\max} = e^{-\xi_r\omega_r(t_2-t_r)}\frac{\sqrt{\left[x_c(t_r)k_c + F_c\right]^2\omega_r^2 + \left[\dot{x}_c(t_r)k_{\text{new}} - (x_c(t_r)k_c + F_c)\xi_r\omega_r\right]^2}}{\omega_r k_{\text{new}}} + \frac{F_c + k_c x_c(t_r)}{k_{\text{new}}} \tag{16}$$

with $x_c(t_r) = l_c - l_r$ and the associated time

$$t_2 = \omega_r^{-1}\tan^{-1}\left[\frac{\dot{x}_c(t_r)k_{\text{new}}\sqrt{1-\xi_r^2}}{-F_c\omega_r - k_c x_c(t_r)\omega_r + \xi_r k_{\text{new}}\dot{x}_c(t_r)}\right] + t_r \tag{17}$$

where ξ_r and ω_r are the modified damping ratio and damped frequency, respectively, with regard to the new stiffness element k_{new}.

A nondimensional analytical solution is then defined to represent the structure–cladding displacement

$$H_{cb}(\lambda) = \frac{x_{c,\max}}{\hat{p}_b/k_{se}} \tag{18}$$

and two additional nondimensional analytical solutions are used to facilitate the sizing of the rubber bumper

$$H_{r1}(\lambda) = \frac{x_{r,\max}}{\hat{p}_b/k_{se}} \tag{19a}$$

$$H_{r2}(\lambda) = \frac{I_{\text{cladding}}}{I_{\text{blast}}} = \frac{m_c\dot{x}_c(t_r)}{(1/2)\hat{p}_b t_p} \tag{19b}$$

where the frequency ratio $\lambda = \Omega/\omega_s$ with the excitation frequency defined as $\Omega = 2\pi/t_p$, $\dot{x}_c(t_r)$ is the velocity of the cladding when impacting with the rubber bumper at $t = t_r$, I_{cladding} is the momentum of the cladding at $t = t_r$, and I_{blast} is the initial impulse of the blast load.

3.2.2. Wind and Seismic Loads. To enable the MBD design, nondimensional transfer functions representing the system's dynamics under harmonic loads are derived based on the above equations of motion. Under harmonic excitations of $p_{w,i} = \hat{p}_{w,i}e^{j\Omega t}$ and $a_g(t) = \hat{a}_g e^{j\Omega t}$, the steady state response of the equivalent structure–cladding system has the following form (Connor and Laflamme, 2014)

$$q_{s1} = \hat{q}_{s1}e^{j(\Omega t+\delta_s)} \tag{20a}$$

$$q_{c1,i} = \hat{q}_{c1,i}e^{j(\Omega t+\delta_{ci})} \tag{20b}$$

where the hat denotes an amplitude, j is the imaginary unit, and δ are the phase angles. Following the derivation in the previous work (Connor and Laflamme, 2014; Gong et al., 2019a, 2019b), the nondimensional transfer functions $H_s(\lambda)$ and $H_{c,i}(\lambda)$ representing the dynamic amplification of the displacement of the SDOF structure and of the displacement of the ith cladding relative to its connected floor are, respectively, written

$$H_{sw}(\lambda) = \frac{\hat{q}_{s1}e^{j\delta_s}}{\hat{p}_e/k_{se}} = \frac{f^2 + j2\xi_c f\lambda}{\left(1-\lambda^2\right)\left(f^2-\lambda^2\right) - 4\xi_c\xi_s f\lambda^2 - \mu\Gamma_2 f^2\lambda^2 + j\left[2\xi_c f\lambda\left(1-(1+\mu\Gamma_2)\lambda^2\right) + 2\xi_s\lambda\left(f^2-\lambda^2\right)\right]} \tag{21}$$

$$H_{cw,i}(\lambda) = \frac{\hat{q}_{c1,i}e^{j\delta_{ci}}}{\hat{p}_e/k_{se}} = \frac{\hat{p}_{w,i}/\hat{p}_e + \alpha_i\mu\lambda^2 H_{sw}(\lambda)}{\mu\left(f^2-\lambda^2\right) + j2\xi_c\mu f\lambda} \tag{22}$$

$$H_{ss}(\lambda) = \frac{\hat{q}_{s1}e^{j\delta_s}}{m_{se}\hat{a}_g/k_{se}} = -\frac{\mu\Gamma_1 f^2 + (f^2-\lambda^2)\Gamma_m + j2\xi_c f\lambda(\mu\Gamma_1+\Gamma_m)}{(1-\lambda^2)(f^2-\lambda^2) - 4\xi_c\xi_s f\lambda^2 - \mu\Gamma_2 f^2\lambda^2 + j\left[2\xi_c f\lambda\left(1-(1+\mu\Gamma_2)\lambda^2\right) + 2\xi_s\lambda(f^2-\lambda^2)\right]} \tag{23}$$

$$H_{cs,i}(\lambda) = \frac{\hat{q}_{c1,i}e^{j\delta_{ci}}}{m_{se}\hat{a}_g/k_{se}} = \frac{\alpha_i\lambda^2 H_{ss}(\lambda) - 1}{f^2-\lambda^2+j2\xi_c f\lambda} \tag{24}$$

where the second subscripts w (wind) and s (seismic) denote the hazard, $\hat{p}_e = \sum_{i=1}^{n}\alpha_i\hat{p}_{w,i}$ the amplitude of the equivalent load, $\Gamma_1 = \sum_{i=1}^{n}\alpha_i$, $\Gamma_2 = \sum_{i=1}^{n}\alpha_i^2$, $\Gamma_m = \sum_{i=1}^{n}\Phi_{s,1i}m_{si}/m_{se}$, μ is the mass ratio, f is the tuning frequency ratio, and λ is the excitation frequency ratio between the cladding and the structure

$$\mu = \frac{m_{ce}}{m_{se}}; \quad f = \frac{\omega_c}{\omega_s}; \quad \text{and} \quad \lambda = \frac{\Omega}{\omega_s} \tag{25}$$

with

$$\omega_s = \sqrt{\frac{k_{se}}{m_{se}}}; \quad \xi_s = \frac{c_{se}}{2m_{se}\omega_s}; \quad \omega_c = \sqrt{\frac{k_{ce}}{m_{ce}}}; \quad \text{and} \quad \xi_c = \frac{c_{ce}}{2m_{ce}\omega_c}$$

An additional transfer function $H_{aw}(\lambda)$ representing the dynamic amplification of the structural acceleration under forcing is given by

$$H_{aw}(\lambda) = \frac{\hat{a}_{s1}e^{j\delta_s}}{\hat{p}_e/m_{se}} = -\lambda^2 H_{sw}(\lambda) \tag{26}$$

where $\hat{a}_{s1} = \Omega^2\hat{q}_{s1}$ denotes the amplitude of the acceleration.

4. Motion-based design procedure

The proposed MBD procedure for the semi-active cladding connection under multihazards is illustrated in Figure 4. It is conducted as follows:

1. First, the multihazard loads are quantified using analytical load models from Section 4.1.
2. Second, the performance objectives are specified for each hazard, including the motion criteria for the primary structure (the peak interstory drift ratio Δ_p and peak structural acceleration a_p) and the cladding element (the allowable structure–cladding spacing l_c).
3. Third, the cladding connection (k_{ce} and ξ_c) is initially designed under wind and seismic loads for a prescribed rubber–cladding spacing $l_{cr} \leqslant l_c$. The rubber–cladding spacing l_{cr} is selected such that the rubber bumper would be used to dissipate impulsive blast energy when necessary, but not to collide with the cladding panel under wind and seismic loads. The peak structural responses under wind and seismic loads are then computed through nondimensional analytical solutions and compared against the corresponding performance objectives.
4. Fourth, the maximum drift ratio $\Delta_{w,\max}$, maximum structural acceleration $a_{\max}$, and maximum cladding displacement relative to the structure $l_{cr,\max}$ under the wind load are computed using nondimensional analytical solutions $R_{s,w}$, $R_{a,w}$, and $R_{c,w}$, respectively, and the maximum drift ratio $\Delta_{s\max}$ and the maximum cladding displacement relative to the structure $l_{cr,\max}$ under the seismic load are computed using nondimensional analytical solutions $R_{s,s}$, and $R_{c,s}$, respectively. Note that $R_{s,w}$, $R_{a,w}$, and $R_{c,w}$ are response factors of floor displacement, acceleration, and cladding displacement under wind load, respectively, and $R_{s,s}$, and $R_{c,s}$ are response factors of floor and cladding displacement under seismic load, respectively. Those response factors are computed as the ratio of the maximum dynamic response to the static response.
5. Fifth, the performance metrics ($\Delta_{s,\max}$, $\Delta_{w,\max}$, $a_{\max}$, and $l_{cr,\max}$) are verified. If one or many performance metric does not comply, an iterative process is conducted where one would choose between updating the allowable structure–cladding spacing l_c (option 1), adjusting the prescribed rubber–cladding spacing l_{cr} (option 2), or redesigning connection parameters k_{ce} and ξ_c (option 3). The blast load design is completed by sizing the rubber bumper parameters, including the prescribed rubber thickness $l_r = l_c - l_{cr}$ and rubber stiffness k_r. It is conducted via the iterative estimation of the maximum rubber deformation $x_{r,\max}$ using H_{cb}, H_{r1}, and H_{r2} and comparing against the allowable rubber deformation $x_{r,u} = 0.8l_r$. Note that these rubber parameters (rubber thickness l_r and rubber stiffness k_r) are to be determined heuristically and that no optimization is performed.

It must be noted that the cladding elements act as light tuned mass dampers and that the relative structure–cladding displacements can be significant (Anajafi and Medina, 2018a; Tributsch and Adam, 2012). It follows that the allowable structure–cladding spacing l_c becomes an important design consideration. Also, the design method is described considering a single wind, seismic, and blast, but could be easily extended to multiwind, multiseismic, and multiblast by conducting the process for every load under consideration and sizing parameters for the governing events.

Under this MBD approach, the VFCC is assumed passive, despite its semi-active capability under wind and seismic events. Such design strategy is common in sizing a target damping capacity of high-performance control systems (Cao et al., 2015; Downey et al., 2016; Hiemenz et al., 2008;

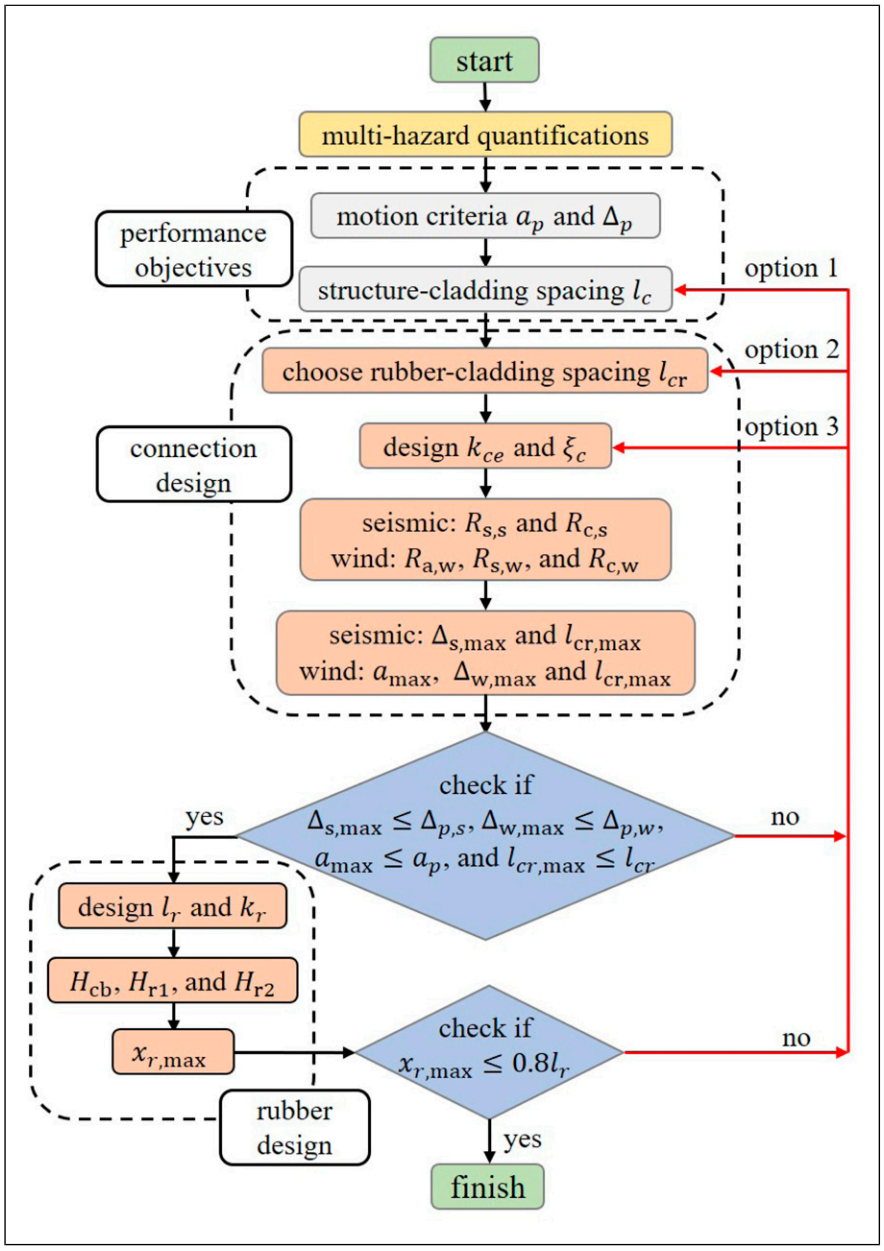

Figure 4. Motion-based design procedure.

Scruggs and Iwan, 2003). The rubber dynamics is linearized using an equivalent stiffness element during the design phase. The accuracy of these assumptions has been verified in the prior work (Cao et al., 2018b; Gong et al., 2019a, 2019b). These simplifications yield trackable analytical solutions, which are necessary to give engineers tools to quickly select dynamic parameters at design stage. Each step of the MBD procedure is described in what follows.

4.1. Hazard quantification

This subsection presents the analytical models for the blast, wind, and seismic loads, which will be used along with transfer functions to compute the peak system responses. Detailed analytical models and derivations of transfer functions can be found in the previous work (Cao et al., 2018b; Gong et al., 2019a, 2019b). Briefly, the design air blast pressure is determined based on the explosive charge weight represented as an equivalent Trinitrotoluene (TNT) mass of W in kg and the standoff distance R between the blast source and the target in meters. The time-varying wind load $P_w(t)$ acting on cladding panels is expressed as the sum of a mean static wind force component P and a fluctuating wind force component $p_w(t)$. The fluctuating wind forces $p_w(t)$ are modeled as a zero-mean Gaussian stationary and spatiotemporal field with its cross-spectral density function obtained

from a two-sided power spectral density function (PSDF) of the fluctuating wind speed (Li et al., 2011). The seismic acceleration is modeled as a zero-mean Gaussian stationary process characterized by a one-sided PSDF $G(\Omega)$ in the frequency domain (Giaralis and Spanos, 2010; Martínez et al., 2013; Vanmarcke, 1975). A discrete PSDF $G(\Omega_N)$ is computed using the design response spectrum $S_g(\Omega_N, \xi_g)$ in ASCE 7–16 (ASCE, 2016; Cacciola et al., 2004; Giaralis and Spanos, 2010).

4.2. Performance objectives

The motion criteria for the wind design are associated with the average return period of the wind excitation (e.g. 1, 10, 50, and 475 years). The commonly used criteria consist of the drift ratio Δ_p that is selected to minimize structural damage and the allowable acceleration a_p that is linked to building serviceability. Taking steel moment-resisting frame structures as an example, typical values for Δ_p are within the range $1/750 \leq \Delta_p \leq 1/250$ (Chan and Wong, 2008) to ensure serviceability over any wind loads' return periods and its exact threshold is left to the designer. The acceptable range for a_p is used on the basis of Li et al. (2004) to ensure occupancy comfort. In particular, the threshold a_p (m s^{-2}) is expressed as a function of the average return period Q (year) and the fundamental frequency of the structure f_s (Hz) (Li et al., 2004)

$$a_p = (0.68 + 0.2 \ln Q)\sqrt{2 \ln(f_s T)}\, e^{-3.65 - 0.41 \ln f_s} \tag{27}$$

where $T = 3600$ s (1 h) is a typical observation time of the wind event.

The performance criteria for seismic-induced motions are generally quantified on structural damage states and interstory drift limits. Cha et al. (2014) list the criteria for typical steel moment-resisting framed structures that allow the selection of drift ratio limits as a function of desired performance levels. For blast-resistant design, the semi-active cladding systems are used to dissipate blast energy and reduce blast-induced vibrations, with the rubber bumper designed within its ultimate compression capacity and the cladding–structure displacement within its performance criterion. No other criterion is used. A prescribed performance level regarding structural motion is not typically considered in current design practices (Cao et al., 2018b). Remark that the prescribed performance objectives could be different. For instance, reducing acceleration during a seismic event can be a critical performance objective because acceleration-induced damage to nonstructural components and building contents can cause significant economic losses.

The structure–cladding spacing must accommodate the installation and maintenance of the lateral cladding connectors. A minimum structure–cladding spacing is often required, and its value can be as high as 15 cm (Pinelli et al., 1995). A maximum upper bound for the structure–cladding gap using enhanced flexible connections can be set as high as 1 m based on values reported in Fu and Zhang (2016). To accommodate a large cladding–structure displacement, a new cladding connection system including a sliding rail, for instance, would replace the traditional stiff connection. The new cladding connection system would be designed to dissipate energy through elastic deformations under wind and seismic events with the cladding panel assumed to be rigid and sustaining no damage, thus requiring no replacement after these hazards. In the case where the cladding panel would sustain damage, it would de facto absorb an certain level of energy, therefore making the design approach conservative despite that necessary costs associated with repairing the broken elements.

4.3. Connection design

The cladding connection design process consists of iteratively selecting dynamic parameters until the performance metrics are achieved under the design loads. A crucial step in this process is the computation of the peak building response and its comparison against the performance criteria. These nondimensional analytical solutions for the peak building response are presented in the previous work (Cao et al., 2018b; Gong et al., 2019a, 2019b).

The cladding connection parameters (k_c and ξ_c) are selected based on the nondimensional analytical solutions under wind and seismic loads, whereas the rubber bumper properties (k_r and l_r) are determined under the blast load. To start, an initial value for the stiffness k_{ce} is determined by selecting a tuning frequency ratio f

$$k_{ce} = \mu f^2 k_{se} \tag{28}$$

Second, the damping ratio of the cladding connection ξ_c is chosen by minimizing the interstory drift ratio under f. An estimated value for ξ_c is computed by setting $\partial R_{s,s}/\partial \xi_c = 0$, where $R_{s,s}$ is the analytical solution associated with the maximum drift ratio $\Delta_{s,\max}$ under the seismic load, derived in the previous work (Gong et al., 2019b). For simplicity, structural damping is taken as $\xi_s = 0$ and setting $\partial R_{s,s}/\partial \xi_c = 0$ yields

$$\xi_c = \sqrt{\frac{(1+\mu\Gamma_2)f^2}{4} + \frac{\Gamma_m^2}{4(1+\mu\Gamma_2)(\mu\Gamma_1+\Gamma_m)^2 f^2} + \frac{(\mu\Gamma_1+\Gamma_m)\mu\Gamma_2 - 2\Gamma_m(1+\mu\Gamma_2)}{4(1+\mu\Gamma_2)(\mu\Gamma_1+\Gamma_m)}} \tag{29}$$

Note that structural damping is not considered to be negligible ($\xi_s \neq 0$) when computing the peak building responses using the analytical solutions. After selecting initial values for the stiffness and damping of the cladding connection, the peak building responses are computed under both design wind and seismic loads and compared against

their prescribed performance objectives. If the motion criteria are satisfied, the design phase for seismic and wind is completed. Otherwise, an iteration is required by selecting either of the three design options (Figure 4). Afterward, the friction damping capacity F_{cp} at each connection is obtained using the equivalent viscous damping concept (Gong et al., 2019a)

$$F_{cp} = \frac{1}{4}\pi m_{ce}\omega_c\omega_s(\xi_c - \xi_{c0})l_{cr} \tag{30}$$

where $\xi_{c0} = (c_{c0}/2m_{ce}\omega_c)$ and the friction damping F_{cp} is equivalent to a viscous damping element under a harmonic excitation acting on the first natural frequency of the structure ω_s and the amplitude of structure–cladding displacement taken as $\hat{x}_c = l_{cr}$.

The connection parameters of the rubber bumper (l_r and k_r) are finalized under the blast load. The maximum structure–cladding displacement $x_{c,\max}$ without considering the rubber bumper is computed and compared against the performance objective l_{cr}. It is obtained by substituting k_c and F_{cp} into the analytical solution H_{cb} (equation (18)). If $x_{c,\max} \le l_{cr}$, the cladding will not collide with the structure, and a minimum rubber thickness l_r is used based on fail-safe requirements. Otherwise, the rubber thickness l_r will be resized to dissipate blast energy with a prescribed maximum rubber deformation $x_{r,\max}$ computed using nondimensional solutions H_{r1} and H_{r2} (equation (19)). To prevent the impact rubber bumper from deforming into its yielding state, the maximum rubber indentation $x_{r,\max}$ is compared against the ultimate compression capacity $x_{r,u} = 0.8l_r$. If $x_{r,\max} \le x_{r,u}$ is satisfied, the design procedure is completed for the blast load.

5. Numerical simulations

5.1. Methodology

5.1.1. Example structures. Two steel moment-resisting frame structures are used to numerically verify and demonstrate the proposed MBD procedure for multihazards. These two buildings, a 9-story and a 20-story building, are taken from the literature (Ohtori et al., 2004) and modeled as lumped-mass shear buildings. Stiffness-proportional Rayleigh damping is used with the inherent first modal damping ratio which is taken as $\xi_s = 2\%$ for each building. The first three modal periods of the structures are 2.27 s, 0.79 s, and 0.49 s for the 9-story building and 3.78 s, 1.37 s, and 0.83 s for the 20-story building. The cladding elements are concrete panels with 30% window open area, with a total length of 45.75 m and 36.6 m at each floor of the 9-story and 20-story building, respectively (Ohtori et al., 2004). The densities of the concrete and glass window panels are taken as 2,400 kg/m^3 and 2,800 kg/m^3, respectively, and their thicknesses are 20 cm and 1 cm, respectively, yielding the cladding mass and cladding-floor mass ratios m_{ci}/m_{si} for each building. A typical cladding-floor mass ratio m_{ci}/m_{si} ranges from 0.01 to 0.1, and previous parametric studies show that an increasing mass ratio m_{ci}/m_{si} improves the mitigation performance for structural response (Gong et al., 2019a, 2019b), analogous to other research findings (Anajafi and Medina, 2018c; Hoang et al., 2008). The cladding mass is generally varied by using different materials (e.g. glass, masonry, or precast concrete). Note that the cladding-floor mass ratios m_{ci}/m_{si} defined here are different from the modal mass ratio $\mu = m_{ce}/m_{se}$ where m_{se} and m_{ce} refer to the modal mass of the structure and cladding in transfer functions (Gong et al., 2019a, 2019b).

5.1.2. Numerical method. The equations of motion of an n-story building equipped with a cladding system have the form

$$\mathbf{M}\ddot{\mathbf{x}} + \mathbf{C}\dot{\mathbf{x}} + \mathbf{K}\mathbf{x} = -\mathbf{M}\mathbf{E}_g a_g + \mathbf{E}_w\mathbf{p}_w + \mathbf{E}_b\mathbf{p}_b + \mathbf{E}_f\mathbf{F} \tag{31}$$

where $\mathbf{x} \in \mathbb{R}^{3n\times 1} = [\mathbf{x}_s; \mathbf{x}_c]$ is the displacement vector with $\mathbf{x}_s \in \mathbb{R}^{n\times 1}$ and $\mathbf{x}_c \in \mathbb{R}^{2n\times 1}$ being the displacement vectors of the structural floors relative to the ground and of the cladding elements relative to the connected structural floors, respectively. $\mathbf{M} \in \mathbb{R}^{3n\times 3n}$, $\mathbf{C} \in \mathbb{R}^{3n\times 3n}$, and $\mathbf{K} \in \mathbb{R}^{3n\times 3n}$ are the mass, damping, and stiffness matrices of the building, respectively, and $\mathbf{E}_g \in \mathbb{R}^{3n\times 1}$, $\mathbf{E}_w \in \mathbb{R}^{3n\times n}$, $\mathbf{E}_b \in \mathbb{R}^{3n\times 2n}$, and $\mathbf{E}_f \in \mathbb{R}^{3n\times 2n}$ are the location matrices for the ground acceleration a_g, wind load vector $\mathbf{p}_w \in \mathbb{R}^{n\times 1}$, blast load vector $\mathbf{p}_b \in \mathbb{R}^{2n\times 1}$, and control input vector $\mathbf{F} \in \mathbb{R}^{2n\times 1}$, respectively.

The state-space representation of equation (31) for the simulations is written

$$\dot{\mathbf{X}} = \mathbf{A}\mathbf{X} + \mathbf{B}_g a_g + \mathbf{B}_w\mathbf{p}_w + \mathbf{B}_b\mathbf{p}_b + \mathbf{B}_f\mathbf{F} \tag{32}$$

where $\mathbf{X} = [\mathbf{x} \quad \dot{\mathbf{x}}]^{\mathrm{T}} \in \mathbb{R}^{6n\times 1}$ is the state vector and with

$$\mathbf{A} = \begin{bmatrix} \mathbf{0} & \mathbf{I} \\ -\mathbf{M}^{-1}\mathbf{K} & -\mathbf{M}^{-1}\mathbf{C} \end{bmatrix}_{6n\times 6n}; \quad \mathbf{B}_f = \begin{bmatrix} \mathbf{0} \\ \mathbf{M}^{-1}\mathbf{E}_f \end{bmatrix}_{6n\times 2n}$$

$$\mathbf{B}_g = \begin{bmatrix} \mathbf{0} \\ -\mathbf{E}_g \end{bmatrix}_{6n\times 1}; \quad \mathbf{B}_w = \begin{bmatrix} \mathbf{0} \\ \mathbf{M}^{-1}\mathbf{E}_w \end{bmatrix}_{6n\times n}; \quad \text{and}$$

$$\mathbf{B}_b = \begin{bmatrix} \mathbf{0} \\ \mathbf{M}^{-1}\mathbf{E}_b \end{bmatrix}_{6n\times 2n}$$

The numerical algorithm follows the discrete form of the Duhamel integral (Connor and Laflamme, 2014)

$$\mathbf{X}(t+\Delta_t) = e^{\mathbf{A}\Delta_t}\mathbf{X}(t) + \mathbf{A}^{-1}\left(e^{\mathbf{A}\Delta_t} - \mathbf{I}\right)\left[\mathbf{B}_f\mathbf{F}(t) + \mathbf{B}_g a_g(t) + \mathbf{B}_w\mathbf{p}_w(t) + \mathbf{B}_b\mathbf{p}_b(t)\right] \tag{33}$$

where Δ_t is the discrete-time interval and $\mathbf{I} \in \mathbb{R}^{6n\times 6n}$ is the identity matrix. Note that this discrete state-space linear formulation is used to simulate the dynamic responses of the buildings assuming linear behaviors. Although nonlinear

structural performance may be expected for the uncontrolled (UN) buildings, its effect on structural response has been found negligible if the structure remains close to linear (Ray-Chaudhuri and Hutchinson, 2011). The nonlinear damping force $\mathbf{F}(t)$ from the VFCC is simulated using the LuGre friction model (Gong et al., 2018).

5.1.3. Control system. A linear quadratic regulator (LQR) controller with full state feedback is used to compute the required control force vector $\mathbf{F}_{\text{req}}$ for the VFCCs under the semi-active control state

$$\mathbf{F}_{\text{req}} = -\mathbf{G}_f \mathbf{X} \tag{34}$$

with the control gain matrix $\mathbf{G}_f \in \mathbb{R}^{2n\times 6n}$ tuned to minimize the performance objective index J_{LQR}

$$J_{\text{LQR}} = \frac{1}{2}\int_0^\infty \left(\mathbf{X}^{\text{T}}\mathbf{R}_x\mathbf{X} + \mathbf{F}^{\text{T}}\mathbf{R}_f\mathbf{F}\right)dt \tag{35}$$

where $\mathbf{R}_x \in \mathbb{R}^{6n\times 6n}$ and $\mathbf{R}_f \in \mathbb{R}^{2n\times 2n}$ are the regulatory and actuation weight matrices, respectively. For a given VFCC device of capacity F_{cp}, the required control force $F_{\text{req},i}(t)$ is not necessarily attainable and a bang-bang type controller is adopted to produce the actual control force $F_{\text{act},i}(t)$ with

$$F_{\text{act},i}(t) = \begin{cases} F_{\text{req},i}(t) & \text{if} \quad F_{cp} > \left|F_{\text{req},i}(t)\right| \quad \text{and} \quad F_{\text{req},i}(t)\dot{x}_{c,i}(t) > 0 \\ F_{cp} & \text{if} \quad F_{cp} \le \left|F_{\text{req},i}(t)\right| \quad \text{and} \quad F_{\text{req},i}(t)\dot{x}_{c,i}(t) > 0 \\ 0 & \text{if} \quad F_{\text{req},i}(t)\dot{x}_{c,i}(t) \le 0 \end{cases} \tag{36}$$

Afterward, a corresponding voltage is obtained based on the actual control force $F_{\text{act},i}(t)$ of the device and sent to the linear actuator acting on the toggles, yielding the kinetic friction force $F_{c,i}(t) = F_{\text{act},i}(t)$. An optimal design of the controller is out of the scope of this work, and the regulatory and actuation weight matrices are pretuned to $\mathbf{R}_x = \text{diag}[\mathbf{I}_{20\times 20}\ 5\mathbf{I}_{7\times 7}\ 100\mathbf{I}_{3\times 3}\ 10\mathbf{I}_{6\times 6}\ \mathbf{I}_{18\times 18}]$ and $\mathbf{R}_f = 10^{-13} \times \text{diag}[\mathbf{I}_{6\times 6}\ 10\mathbf{I}_{12\times 12}]$ for the 9-story building, and $\mathbf{R}_x = \text{diag} \times [\mathbf{I}_{20\times 20}\ 10\mathbf{I}_{13\times 13}\ 20\mathbf{I}_{17\times 17}\ 40\mathbf{I}_{10\times 10}\ 250\mathbf{I}_{5\times 5}\ 400\mathbf{I}_{10\times 10}\ 100\mathbf{I}_{5\times 5}\ \mathbf{I}_{40\times 40}]$ and $\mathbf{R}_f = 5 \times 10^{-12}\text{diag}[\mathbf{I}_{10\times 10}\ 10\mathbf{I}_{10\times 10}\ 50\mathbf{I}_{20\times 20}]$ for the 20-story building. The semi-active simulation case (LQR) is compared against the ON case where the VFCC is used under a constant maximum capacity and the UN case where the cladding is attached using a conventional lateral stiffness connection. These stiffness connections used in the UN case are conventional bearing connectors at the bottom and tie-back connectors at the top of cladding panels, with lateral stiffness of each bearing connector and tie-back connector taken as 2335 KN/mm and 39 KN/mm for the 9-story and 20-story buildings, respectively (Pantoli and Hutchinson, 2015). A total number of 10 connectors and 24 connectors are used at each floor for the 9-story and 20-story buildings, respectively, and the stiffness element of the lateral connection k_c is taken as the sum of these connectors at each floor.

5.1.4. Simulated hazards.

5.1.4.1. Blast load. The blast load is simulated with an amplitude $\hat{p}_b$ computed based on a design explosive charge TNT weight of $W = 200$ kg (approximate explosive mass in the trunk of a large car (Draganić and Sigmund, 2012)) and an arbitrary standoff distance of $R = 25$ m. Parameter values for the design blast load such as load amplitude $\hat{p}_b$, time duration t_p, and standoff distance R are computed at each cladding nodes of the 9-story and 20-story buildings.

5.1.4.2. Wind load. The time series data for the wind speed $v_i(t)$ are simulated as a multivariate stochastic process with the cross-spectral density matrix $\mathbf{S}(\Omega)$ (Kaimal et al., 1972)

$$S_{il}(\Omega) = \begin{cases} S_v(z_i, \Omega) & \text{if } i = l \\ \sqrt{S_v(z_i, \Omega)S_v(z_l, \Omega)}\,\text{Coh}(z_i, z_l, \Omega) & \text{if } i \neq l \end{cases} \tag{37}$$

with the two-sided PSD $S_v(z_i, \Omega)$ and the coherence function $\text{Coh}(z_i, z_l, \Omega)$ from the literature (Li et al., 2011). Time series are generated following the simulation algorithm for ergodic multivariate stochastic processes from Deodatis (1996). The simulated wind load $P_{w,i}(t)$ acting on the cladding panels at the ith floor is generated using

$$P_{w,i}(t) = \frac{1}{2}\rho C_d A_i [V_i + v_i(t)]^2 \tag{38}$$

where V_i is the mean wind speed at building height z_i and the air density is taken as $\rho = 1.225$ kg/m^3. Note that both windward and leeward facades are modeled as a single panel on each floor. Therefore, wind load acting on each cladding panel can be treated as the sum of windward and leeward wind force.

5.1.4.3. Seismic load. A set of six different earthquakes are used for the simulations. Time history data of these ground accelerations were extracted from the PEER ground motion record database (PEER, 2011) and scaled based on the local design response spectrum at the fundamental period of each building. Table 1 shows the dynamic characteristics, and Figure 5 shows the design response spectrum and the scaled response spectrum of each ground motion.

5.2. MBD procedure

5.2.1. Multihazard Quantification. The design blast load is arbitrarily selected as equivalent to a 200 kg mass of TNT (e.g. $W = 200$ kg), which approximately corresponds to a charge located in the trunk of a large car (Draganić and Sigmund, 2012), at a standoff distance of $R = 25$ m.

The wind load is designed based on a 3 s wind gust speed $V_0 = 33$ m/s at a reference height of 10 m with a return period of $Q = 50$ years using the wind hazard map from ASCE 7–16 (ASCE, 2016). A return period of $Q = 50$ years is selected to be consistent with the nominal design wind

Table 1. Selected seismic excitations.

Hazard	Location	Year	Station	Distance (km)	Mechanism	Scale factor	
						9-Story	20-Story
EQ1	Northridge	1994	Ventura Harbor	54.28	Reverse	1.55	3.02
EQ2	Kern county	1952	Santa Barbara	81.3	Reverse	1.18	2.03
EQ3	Landers	1992	Brea	137.44	Strike-slip	1.56	1.75
EQ4	Imperial valley	1979	El Centro Array 8	3.86	Strike-slip	0.55	0.68
EQ5	Chi-Chi	1999	CHY093	49.82	Reverse-oblique	1.67	1.64
EQ6	Kobe	1995	Morigawachi	24.78	Strike-slip	0.89	1.22

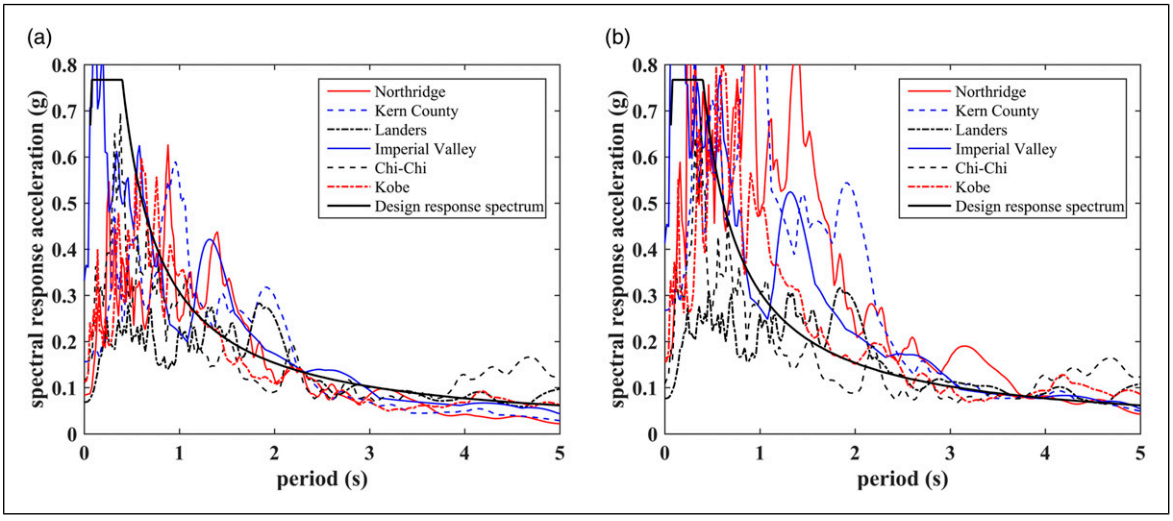

Figure 5. Scaled response spectra of selected seismic excitations: (a) 9-story (fundamental period: T_s = 2.27 s) and (b) 20-story (fundamental period: T_s = 3.78 s) buildings.

speed in nonhurricane regions of the United States (Vickery et al., 2009). The wind loading parameters determined based on the building terrain (suburb) include the ratio of shear velocity of wind flow $v_*/v_{*0} = 1.15$, surface roughness length $z_* = 0.3$ m, and its corresponding $\beta = 5.25$. The drag coefficient is taken as $C_d = 1.4$ and $C_d = 1.3$ for the 9-story and 20-story building, respectively, based on a rectangular building cross section (Simiu and Scanlan, 1996).

The seismic hazard is quantified based on the local design response spectra of the buildings, both located in the state of California with corresponding spectral acceleration parameters $S_{DS} = 0.667$ g and $S_{D1} = 0.267$ g (Cha et al., 2014). Using the seismic load model from Section 4.1, an updated discrete design spectrum compatible PSDF $G_{\text{new}}(\Omega_N)$ can be obtained for design.

5.2.2. Performance Objectives. The performance objectives are prescribed based on hazard types. The allowable structure–cladding spacing l_c is set as 0.45 m and 0.55 m for the 9-story and 20-story building, respectively, for the preliminary design phase, with an upper bound set to 1 m. Under the wind load, the acceptable peak acceleration for occupancy comfort is computed using equation (27) with values $a_p = 22.8$ mg and $a_p = 27.3$ mg for the 9-story and 20-story buildings, respectively, and the allowable lateral drift ratio set to $\Delta_p < 0.4\%$. Under the seismic load, the allowable lateral drift is set to $\Delta_p < 1\%$ to maintain an elastic state (Ray-Chaudhuri and Hutchinson, 2011) within the life safety range as indicated in literatures (Cha et al., 2014; Council, 2000). The cladding connection is designed to prevent the cladding element from colliding with the rubber bumper under wind and seismic loads. Under the blast load, the deformation of the rubber bumper $x_{r,\max}$ is designed to be within its ultimate compression capacity $x_{r,u}$, with $x_{r,\max} \le x_{r,u} = 0.8 l_r$.

5.2.3. Connection Design. Table 2 lists values for the modal mass m_{se} and stiffness k_{se} of the primary structure and the modal mass ratio $\mu = m_{ce}/m_{se}$ used for wind and seismic design, and the mass $m_b = m_c/2$ for blast design at each connection node, where m_c is the cladding mass. The cladding–rubber distances l_{cr} for the design under wind and

Table 2. Cladding connection design parameters.

Parameter	Variable	Unit	Value	
			9-Story	20-Story
Structure parameters	m_{se}	10^3 kg	4528	5057
	k_{se}	KN m^{-1}	34,408	13,971
	μ	%	1.44	1.01
	m_b	kg	43.3	34.6
Motion criteria	$\Delta_{p,s}$	%	0.93	0.86
	$\Delta_{p,w}$	%	0.15	0.27
	a_p	mg	20.3	25.8
	l_c	m	0.45	0.55
Connection parameters	l_r	m	0.15	0.15
	l_{cr}	m	0.3	0.4
	f	—	1.29	1.94
	k_{ce}	KN m^{-1}	822.8	529.1
	ξ_c	—	0.33	0.80
	F_{cp}	KN	27.2	34.3
	k_r	10^6 Nm^{-1}	4114	2645

seismic loads are preselected as 0.3 m and 0.4 m for the 9-story and 20-story buildings, respectively, with a prescribed rubber bumper thickness of l_r = 0.15 m for both buildings. The estimated maximum responses of each building under design wind and seismic loads versus the tuning frequency ratios f are plotted as shown in Figures 6 and 7. From the performance objectives on the peak drift ratio Δ_p, peak acceleration a_p, and structure–rubber spacing l_{cr}, tuning frequency ratios f = 1.29 and f = 1.94 are selected for the 9-story and 20-story buildings, respectively. The selection of the tuning frequency ratio f is governed, for both buildings, by the cladding–rubber spacing l_{cr}. This design yields a connection modal stiffness k_{ce} (equation (28)), connection damping ratio ξ_c (equation (29)), and the total friction damping capacity at each floor F_{cp} (equation (30)). The design parameters are listed in Table 2.

The blast load design is conducted based on three nondimensional analytical solutions. Using these design parameters, the maximum structure–cladding displacement

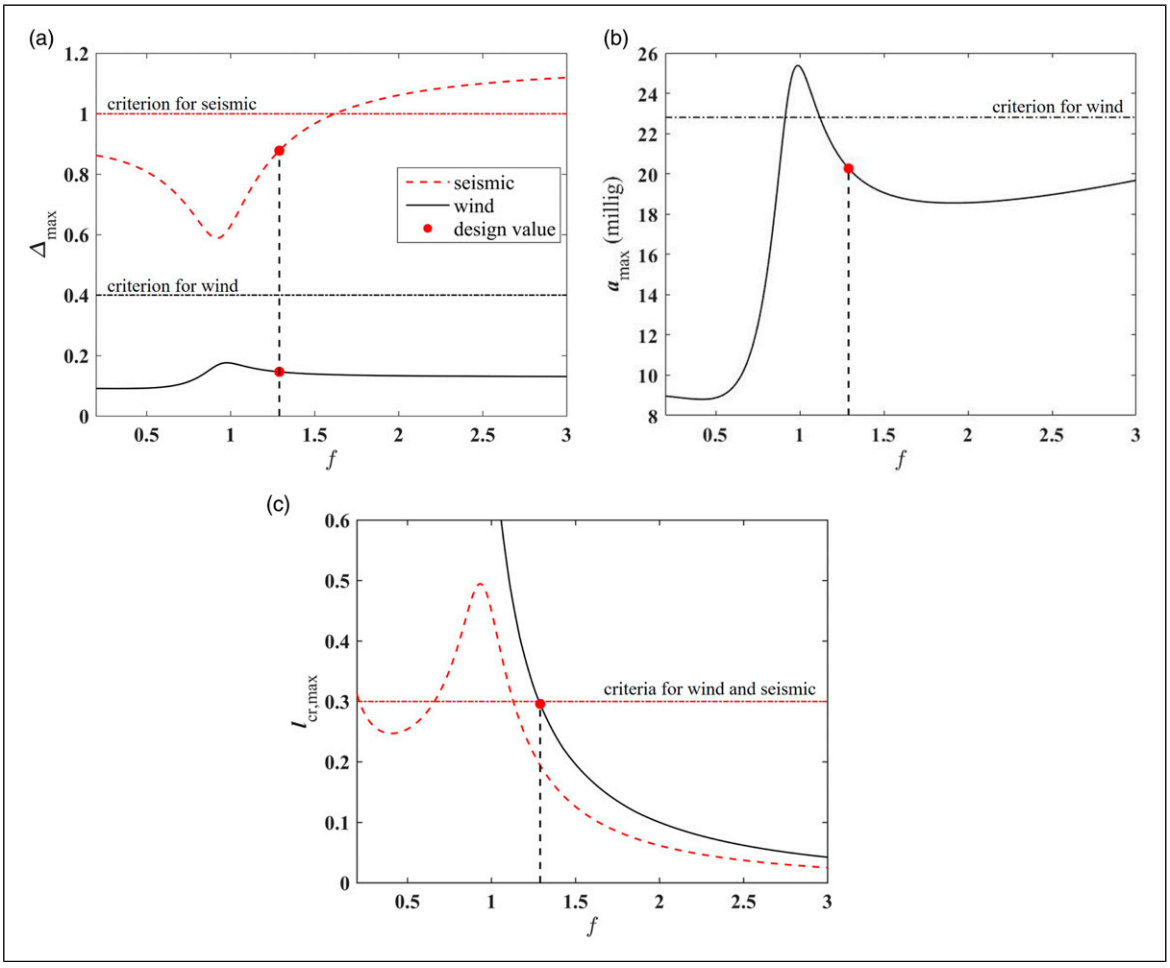

Figure 6. Peak responses of the 9-story building as a function of f: (a) Δ_{max}, (b) a_{max}, and (c) $l_{cr,max}$.

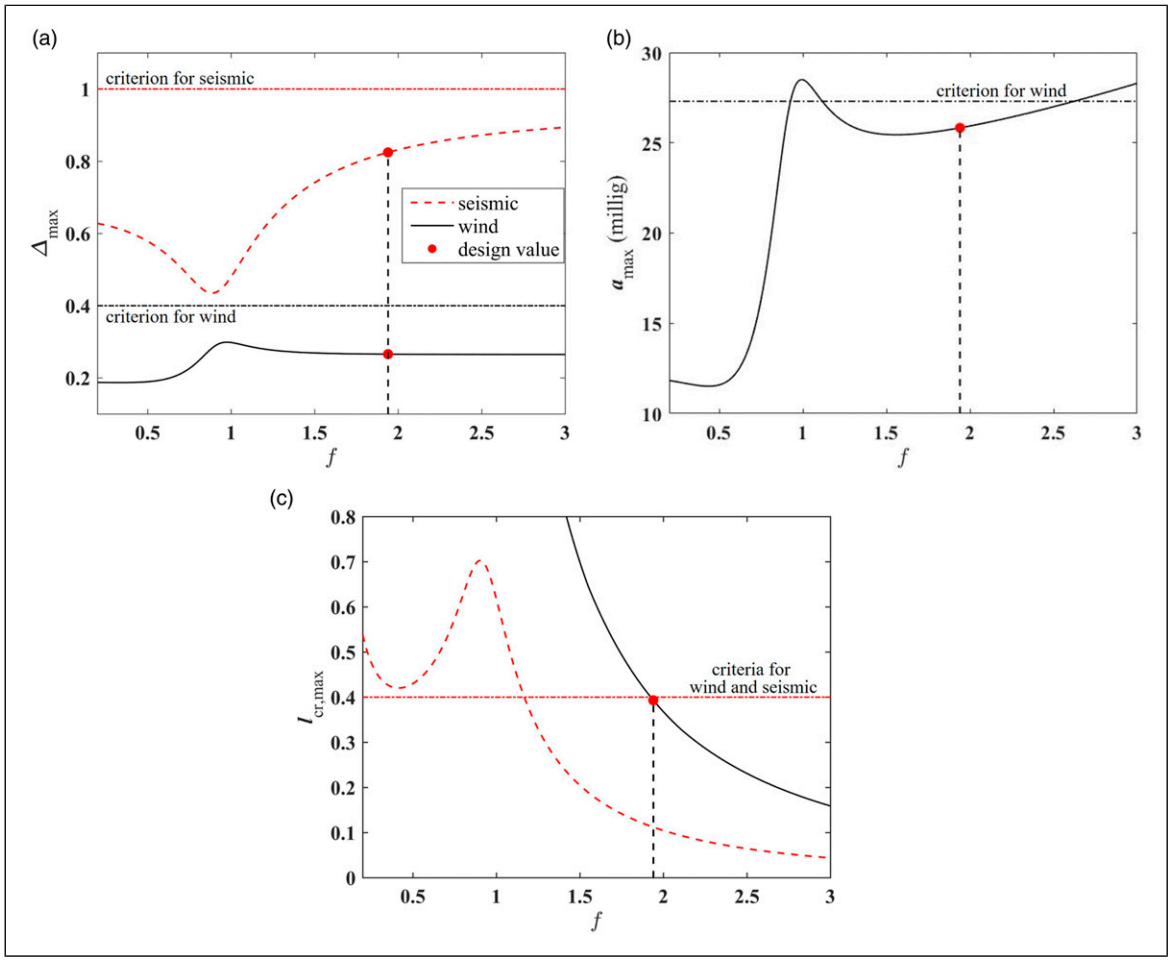

Figure 7. Peak responses of the 20-story building as a function of f: (a) Δ_{max}, (b) a_{max}, and (c) $l_{cr,max}$.

without considering the rubber bumper is estimated as $x_{c,max} = 0.63$ m and $x_{c,max} = 0.66$ with corresponding values for $H_{cb} = 1.75$ and $H_{cb} = 0.095$ for the 9-story and 20-story building, respectively. It shows that $x_{c,max} > l_{cr}$ for both buildings, and the cladding is anticipated to collide with the cladding. With an initial rubber thickness $l_r = 0.15$ m, it yields the values for $H_{r2} = 0.85$ and $H_{r2} = 0.75$ for the 9-story and 20-story building, respectively. Selecting the values for the rubber stiffness $k_r = 10^4 k_c$ at the 9-story building gives $H_{r1} = 0.1833$ and $x_{r,max} = 0.065$ m which meets the requirement that $x_{r,max} = 0.065$ m $< 0.8 l_r = 0.12$ m. Similarly, a rubber stiffness $k_r = 10^4 k_c$ at the 20-story building yields satisfactory performance with $x_{r,max} = 0.062$ m $< 0.8 l_r = 0.12$ m and $H_{r1} = 0.0084$. These rubber parameters are listed in Table 2.

5.3. Numerical verification

The numerical verification consists of verifying the MBD procedure and demonstrating the performance of the VFCC on the two example buildings.

Tables 3 and 4 list results on the performance objectives for the 9-story and 20-story buildings, respectively, including the maximum interstory drift ratio Δ_{max}, maximum acceleration a_{max}, and maximum structure–cladding displacement $l_{cr,max}$. Results show that the passive-on (ON) case, which was used for the MBD procedure, does not always meet the performance objectives. In particular, for the 20-story building, one can observe that $\Delta_{max} = 0.28\% > \Delta_p = 0.27\%$ and $a_{max} = 27$ millig $> a_p = 25.8$ millig under the wind load and $\Delta_{max} = 1.0\% > \Delta_p = 0.86\%$ under EQ5. This disagreement between the numerical results and analytical solutions is attributed to the quality of the assumptions made to develop mathematically trackable solutions, including (1) the negligence of higher modal responses of the structure, (2) the simplification of load inputs, and (3) the negligence of the VFCC's nonlinearities by using an equivalent viscous system (Cao et al., 2018b; Gong et al., 2019a, 2019b). Results show that the quality of these assumptions could be more important for seismic design, as the underestimation of the performance objectives was more notable than under wind. Nevertheless, the semi-active

Table 3. Results for motion performance criteria: 9-story building.

	Δ_{max}(%)			$a_{max}(g)$			$l_{c,max}$ (m)	
Hazard	UN	ON	LQR	UN	ON	LQR	ON	LQR
Wind	0.15	0.14	0.14	0.026	0.019	0.017	0.23	0.26
Blast	0.18	0.14	—	1.98	0.26	—	0.37	—
EQ1	0.66	0.60	0.47	0.16	0.15	0.14	0.06	0.19
EQ2	0.76	0.70	0.62	0.26	0.24	0.22	0.18	0.24
EQ3	0.79	0.74	0.50	0.17	0.15	0.13	0.15	0.19
EQ4	0.85	0.84	0.80	0.27	0.25	0.24	0.16	0.29
EQ5	0.66	0.61	0.50	0.17	0.17	0.16	0.08	0.16
EQ6	0.80	0.73	0.56	0.25	0.24	0.22	0.14	0.20

UN: uncontrolled; ON: passive-on; LQR: linear quadratic regulator.

Table 4. Results for motion performance criteria: 20-story building.

	Δ_{max}(%)			$a_{max}(g)$			$l_{c,max}$ (m)	
Hazard	UN	ON	LQR	UN	ON	LQR	ON	LQR
Wind	0.28	0.28	0.25	0.039	0.027	0.023	0.26	0.36
Blast	0.18	016	—	3.48	0.20	—	0.46	—
EQ1	0.85	0.76	0.54	0.31	0.28	0.19	0.15	0.35
EQ2	0.82	0.79	0.68	0.33	0.31	0.28	0.15	0.27
EQ3	0.80	0.79	0.58	0.16	0.16	0.15	0.02	0.21
EQ4	0.73	0.73	0.69	0.23	0.23	0.23	0.05	0.24
EQ5	1.02	1.00	0.71	0.16	0.16	0.14	0.02	0.23
EQ6	0.81	0.78	0.63	0.21	0.19	0.17	0.03	0.22

UN: uncontrolled; ON: passive-on; LQR: linear quadratic regulator.

VFCC (LQR) meets the quantified structural performance objectives under each hazard, showing that the MBD procedure is largely conservative by assuming a passive behavior of the device (ON case).

The next step is to assess the capability of the VFCC at mitigating structural vibrations. To do so, two performance indices are defined:

1. Maximum interstory drift reduction J_1

$$J_1 = \frac{\max_{i,t}|\Delta_{un,i}(t)| - \max_{i,t}|\Delta_i(t)|}{\max_{i,t}|\Delta_{un,i}(t)|} \tag{39}$$

where the controlled interstory drift ratio $\Delta_i = (x_{s,i} - x_{s,i-1})/h_i$ for $i = 2, 3, \ldots, n$, $\Delta_1 = x_{s,1}/h_1$ for $i = 1$ and $\Delta_{un,i}$ refers to the UN interstory drift ratio.

2. Maximum absolute acceleration reduction J_2

$$J_2 = \frac{\max_{i,t}|\ddot{x}_{un,i}(t)| - \max_{i,t}|\ddot{x}_i(t)|}{\max_{i,t}|\ddot{x}_{un,i}(t)|} \tag{40}$$

Table 5. Simulation results: J_1 and J_2.

	9-Story building				20-Story building			
	J_1(%)		J_2(%)		J_1(%)		J_2(%)	
Hazard	ON	LQR	ON	LQR	ON	LQR	ON	LQR
Wind	3.6	4.4	29.6	35.1	0.1	13.0	29.0	39.6
Blast	13.4	—	85.6	—	10.4	—	94.8	—
EQ1	8.5	32.9	4.4	13.2	7.0	21.8	10.3	37.6
EQ2	6.6	19.0	4.7	14.4	2.1	15.6	6.0	15.7
EQ3	5.2	36.3	8.2	21.0	1.5	27.0	1.5	7.3
EQ4	3.1	6.9	6.5	9.0	0.8	10.7	1.2	1.2
EQ5	7.0	25.5	0.6	8.4	1.4	28.2	1.3	11.0
EQ6	8.9	29.2	4.7	12.1	4.2	22.2	8.0	19.9

ON: passive-on; LQR: linear quadratic regulator.

where the absolute acceleration $\ddot{x}_i = \ddot{x}_{s,i}$ for $i = 1, 2, \ldots, n$ is the acceleration for the controlled cases and $\ddot{x}_{un,i}$ is the acceleration for the UN case.

Table 5 lists the simulation results for the two performance indices. Positive values for J_1 and J_2 correspond to a mitigation of the load. Results show that under both ON and LQR, the VFCC provides a certain level of mitigation under all hazards. The LQR case exhibits significantly enhanced performance for the vast majority of hazards, except under blast where the semi-active state is not activated. In particular, the maximum reduction of the interstory drift and acceleration under wind load reaches 13% and 39.6%, respectively, for the 20-story building. The lower gain in performance from the LQR strategies under wind for the 9-story building is attributed to the lower dynamic response of the structure to wind excitations. The maximum reduction of the interstory displacement and absolute acceleration reaches 36.3% and 21%, respectively, for the 9-story building under seismic hazard EQ3, and 28.2% under hazard EQ5 and 37.6% under hazard EQ1, respectively, for the 20-story building. The VFCC under both ON and LQR does not mitigate EQ4 significantly, which can be attributed to the earthquake-specific dynamics. The passive-on VFCC under blast loads leads to a maximum 13.4% reduction of the interstory drift for the 9-story building and a maximum 94.8% reduction of the acceleration for the 20-story building.

Figures 8 and 9 show typical maximum response profiles for both buildings under different hazards. The absolute acceleration under wind and blast loads and the drift ratio under the seismic load are selected as examples. The seismic responses of the 9-story and 20-story (Figures 8(b) and 9(b)) buildings are shown under seismic hazard case EQ6, which exhibits an average reduction in the maximum interstory drift ratio compared with the six seismic hazards. Figures 8(a) and 9(a) show that the LQR case significantly outperforms other cases under wind load for acceleration

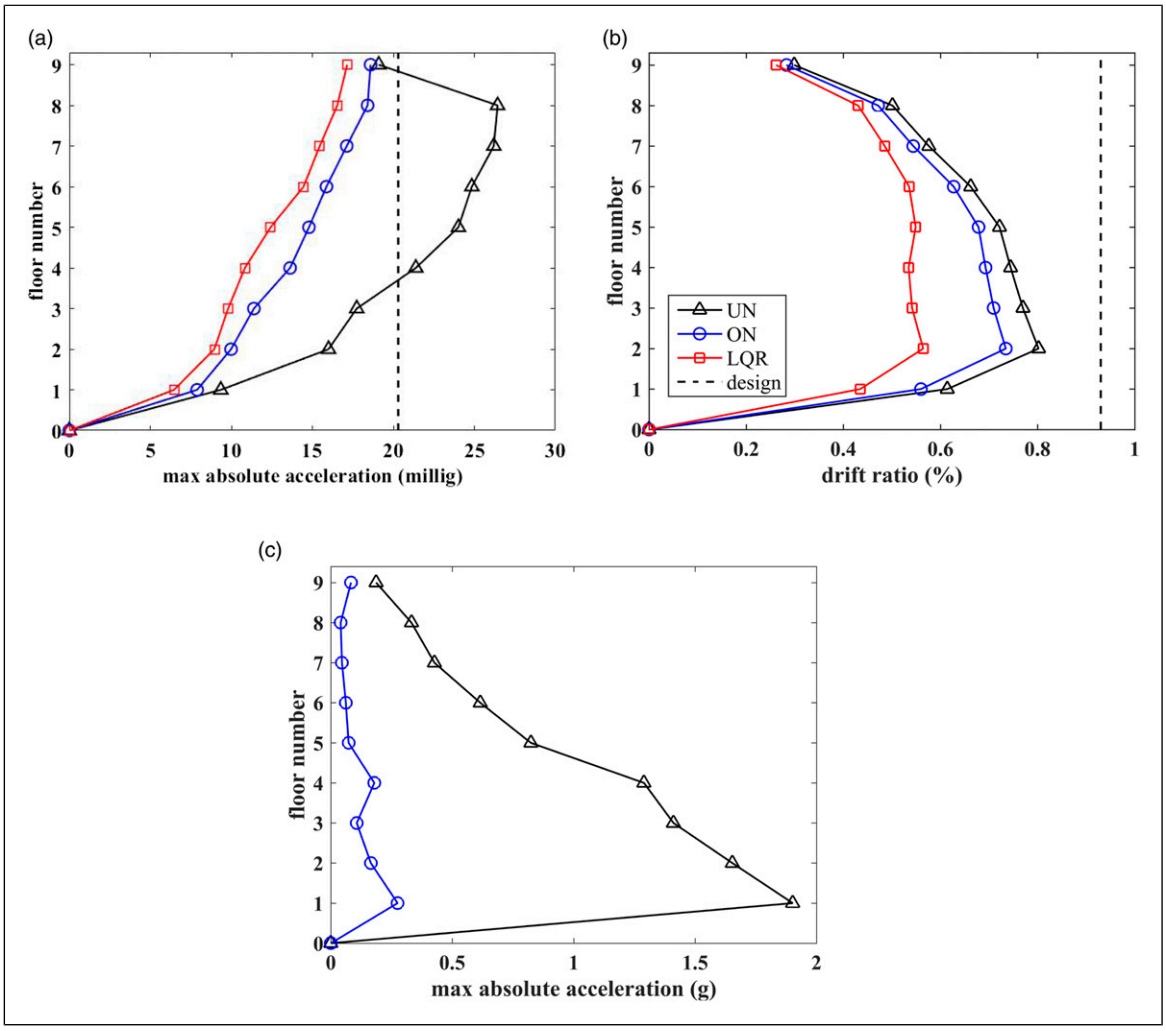

Figure 8. Maximum response profile of the 9-story building: (a) absolute acceleration under wind hazard, (b) drift ratio under hazard EQ6, and (c) absolute acceleration under blast load.

mitigation and meets performance objectives unlike the UN case for both buildings and the ON case for the 20-story building. The LQR case also outperforms under control strategies under seismic (Figures 8(b) and 9(b)), although the performance objectives are already met under the UN case. Results from blast (Figures 8(c) and 9(c)) show a net improvement from using the VFCC in a passive mode, where the most significant mitigation comes from the first floor where the blast load magnitude is the highest. Overall, all profiles show that mitigation is achieved by leveraging a higher structure–cladding displacement and that it is possible to satisfy all performance requirements by keeping this displacement under the prescribed threshold.

6. Conclusion

A novel VFCC has been previously developed by the authors to leverage cladding element motion to mitigate wind, seismic, and blast hazards and MBD procedures developed individually for each of these hazards. This article integrates these results by introducing an MBD procedure when more than one hazard is considered, termed multihazard.

The MBD procedure for multihazard mitigation was described. The procedure starts with the quantification of each hazard under consideration and the performance objectives. It is followed by a selection of the dynamic parameters of the connection under wind and seismic loads, after which the device's impact bumper is designed to satisfy motion requirements under blast. Last, the peak building responses are computed and iterations conducted on the design parameters on the satisfaction of the multiple motion objectives.

Numerical simulations were conducted to verify the proposed MBD methodology and demonstrate the capabilities of the VFCC on two example structures: a 9-story and 20-story building. Multiple hazards were simulated,

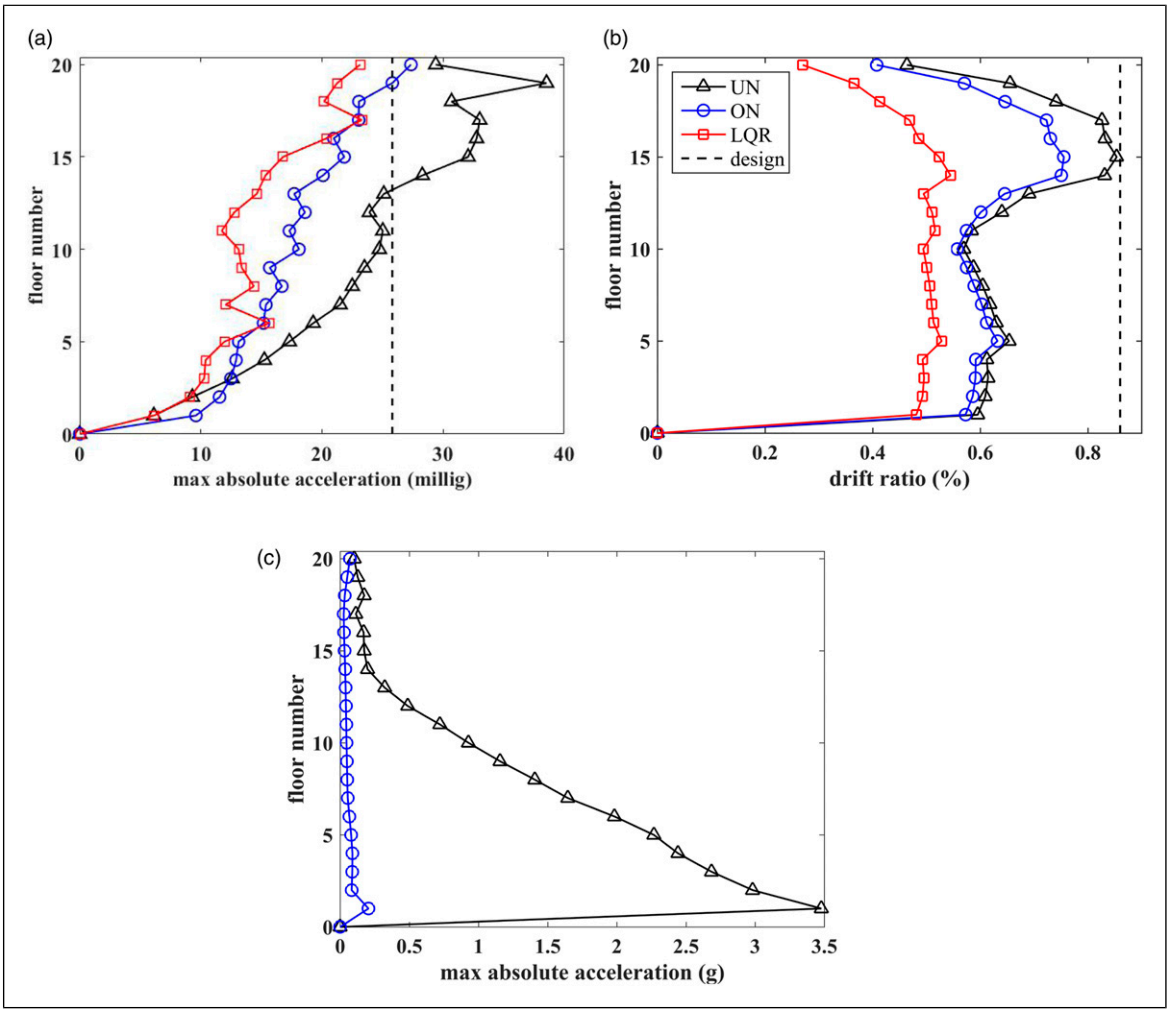

Figure 9. Maximum response profile of the 20-story building: (a) absolute acceleration under wind hazard, (b) drift ratio under hazard EQ6, and (c) absolute acceleration under blast load.

including wind, earthquakes, and blast, and applied to the selected buildings with the designed VFCC under the proposed MBD procedure. Performance was assessed under three control cases: (1) uncontrolled, where the cladding was linked to the structure using conventional elements, (2) passive-on, where the VFCC is permanently set to maximum capacity, and (3) semi-active, where a full state feedback linear quadratic controller is used to determine the control gains. Simulation results showed that the MBD procedure, conducted assuming the ON case, satisfied most of the motion criteria. The assessment of the VFCC performance showed that semi-active control produced significantly enhanced mitigation capabilities compared with the ON case under seismic and wind hazards. Overall, results presented in this article showed that the VFCC is a promising device, capable of mutlihazard mitigation, and that MBD procedures can be integrated at the structural design phase to produce structures capable of high performance versus motion.

Declaration of conflicting interests

The author(s) declared no potential conflicts of interest with respect to the research, authorship, and/or publication of this article.

Funding

The author(s) disclosed receipt of the following financial support for the research, authorship, and/or publication of this article: This material is based on the work supported by the National Science Foundation under Grant No. 1463252 and No. 1463497. Their support is gratefully acknowledged. Any opinions, findings, and conclusions or recommendations expressed in this material are those of the author(s) and do not necessarily reflect the views of the National Science Foundation.

ORCID iD

Liang Cao https://orcid.org/0000-0001-7156-4215

References

Alberdi R, Przywara J and Khandelwal K (2013) Performance evaluation of sandwich panel systems for blast mitigation. *Engineering Structures* 56: 2119–2130.

Amadio C and Bedon C (2012) Viscoelastic spider connectors for the mitigation of cable-supported façades subjected to air blast loading. *Engineering Structures* 42: 190–200.

Anajafi H and Medina RA (2018a) Comparison of the seismic performance of a partial mass isolation technique with conventional TMD and base-isolation systems under broad-band and narrow-band excitations. *Engineering Structures* 158: 110–123.

Anajafi H and Medina RA (2018b) Partial mass isolation system for seismic vibration control of buildings. *Structural Control and Health Monitoring* 25(2): e2088.

Anajafi H and Medina RA (2018c) Robust design of a multi-floor isolation system. *Structural Control and Health Monitoring* 25(4): e2130.

ASCE (2016) *Minimum Design Loads for Buildings and Other Structures*. Reston, VA: American Socitey of Civil Engineering.

Baird A, Palermo A and Pampanin S (2013) Controlling seismic response using passive energy dissipating cladding connections. In: New Zealand society for earthquake engineering conference, Christchurch, New Zealand, 26–28 April 2013.

Bitaraf M, Ozbulut OE, Hurlebaus S, et al. (2010) Application of semi-active control strategies for seismic protection of buildings with MR dampers. *Engineering Structures* 32(10): 3040–3047.

Cacciola P, Colajanni P and Muscolino G (2004) Combination of modal responses consistent with seismic input representation. *Journal of Structural Engineering* 130(1): 47–55.

Cao L, Downey A, Laflamme S, et al. (2015) Variable friction device for structural control based on duo-servo vehicle brake: Modeling and experimental validation *Journal of Sound and Vibration* 348: 41–56.

Cao L, Laflamme S Hong J, et al. (2018a) Input space dependent controller for civil structures exposed to multi-hazard excitations. *Engineering Structures* 166: 286–301.

Cao L, Laflamme S, Taylor D, et al. (2016) Simulations of a variable friction device for multihazard mitigation. *Journal of Structural Engineering* 142(12): H4016001.

Cao L, Lu S, Laflamme S, et al. (2018b) Performance-based design procedure of a novel friction-based cladding connection for blast mitigation. *International Journal of Impact Engineering* 117: 48–62.

Cha Y-J, Agrawal AK, Phillips BM, et al. (2014) Direct performance-based design with 200 kN MR dampers using multi-objective cost effective optimization for steel MRFs. *Engineering Structures* 71: 60–72.

Chan C-M and Wong K-M (2008) Structural topology and element sizing design optimisation of tall steel frameworks using a hybrid OC-GA method. *Structural and Multidisciplinary Optimization* 35(5): 473–488.

Chen W and Hao H (2013a) Numerical study of blast-resistant sandwich panels with rotational friction dampers. *International Journal of Structural Stability and Dynamics* 13(6): 1350014.

Chen WS and Hao H (2013b) Preliminary study of sandwich panel with rotational friction hinge device against blast loadings. *Key Engineering Materials* 535: 530–533.

Connor J and Laflamme S (2014) *Structural Motion Engineering*. Switzerland: Springer, Vol. 493.

Council BSS (2000) *Prestandard and commentary for the seismic rehabilitation of buildings*. Report FEMA-356, Washington, DC.

Dal Lago B, Biondini F and Toniolo G (2018) Experimental investigation on steel w-shaped folded plate dissipative connectors for horizontal precast concrete cladding panels. *Journal of Earthquake Engineering* 22(5): 778–800.

Deodatis G (1996) Simulation of ergodic multivariate stochastic processes. *Journal of Engineering Mechanics* 122(8): 778–787.

Downey A, Cao L, Laflamme S, et al. (2016) High capacity variable friction damper based on band brake technology. *Engineering Structures* 113: 287–298.

Draganić H and Sigmund V (2012) Blast loading on structures. *Technical Gazette* 19(3): 643–652.

Ferrara L, Felicetti R, Toniolo G, et al. (2011) Friction dissipative devices for cladding panels in precast buildings. An experimental investigation. *European Journal of Environmental and Civil engineering* 15(9): 1319–1338.

Filiatrault A, Tremblay R and Wanitkorkul A (2001) Performance evaluation of passive damping systems for the seismic retrofit of steel moment-resisting frames subjected to near-field ground motions. *Earthquake Spectra* 17(3): 427–456.

Fisco N and Adeli H (2011) Smart structures: Part ii-hybrid control systems and control strategies. *Scientia Iranica* 18(3): 285–295.

Fu TS and Zhang R (2016) Integrating double-skin façades and mass dampers for structural safety and energy efficiency. *Journal of Architectural Engineering* 22(4): 04016014.

Giaralis A and Spanos PD (2010) Effective linear damping and stiffness coefficients of nonlinear systems for design spectrum based analysis. *Soil Dynamics and Earthquake Engineering* 30(9): 798–810.

Gong Y, Cao L, Laflamme S, et al. (2018) Characterization of a novel variable friction connection for semiactive cladding system. *Structural Control and Health Monitoring* 25(6): e2157.

Gong Y, Cao L, Laflamme S, et al. (2019a) Motion-based design approach for a novel variable friction cladding connection used in wind hazard mitigation. *Engineering Structures* 181: 397–412.

Gong Y, Cao L, Laflamme S, et al. (2019b) Variable friction cladding connection for seismic mitigation. *Engineering Structures* 189: 243–259.

Guo JWW and Christopoulos C (2013) Performance spectra based method for the seismic design of structures equipped with passive supplemental damping systems. *Earthquake Engineering & Structural Dynamics* 42(6): 935–952.

Hiemenz GJ, Hu W and Wereley NM (2008) Semi-active magnetorheological helicopter crew seat suspension for vibration isolation. *Journal of Aircraft* 45(3): 945–953.

Hoang N, Fujino Y and Warnitchai P (2008) Optimal tuned mass damper for seismic applications and practical design formulas. *Engineering Structures* 30(3): 707–715.

Hong J, Laflamme S, Cao L, et al. (2018) Variable input observer for nonstationary high-rate dynamic systems. *Neural Computing and Applications* 32: 1–12.

Kaimal JC, Wyngaard J, Izumi Y, et al. (1972) Spectral characteristics of surface-layer turbulence. *Quarterly Journal of the Royal Meteorological Society* 98(417): 563–589.

Karagiozova D, Langdon G and Nurick G (2010) Blast attenuation in cymat foam core sacrificial claddings. *International Journal of Mechanical Sciences* 52(5): 758–776.

Kim G and Kang J (2011) Seismic response control of adjacent building by using hybrid control algorithm of mr damper. *Procedia Engineering* 14: 1013–1020.

Larcher M (2008) Pressure-time functions for the description of air blast waves. JRC Technical Note 46829.

Li Q and Meng H (2002) Pressure-impulse diagram for blast loads based on dimensional analysis and single-degree-of-freedom model. *Journal of Engineering Mechanics* 128(1): 87–92.

Li Q, Wu J, Liang S, et al. (2004) Full-scale measurements and numerical evaluation of wind-induced vibration of a 63-story reinforced concrete tall building. *Engineering structures* 26(12): 1779–1794.

Li Q, Zou X, Wu J, et al. (2011) Integrated wind-induced response analysis and design optimization of tall steel buildings using micro-GA. *The Structural Design of Tall and Special Buildings* 20(8): 951–971.

Ma G and Ye Z (2007) Energy absorption of double-layer foam cladding for blast alleviation. *International Journal of Impact Engineering* 34(2): 329–347.

Maneetes H and Memari A (2014) Introduction of an innovative cladding panel system for multi-story buildings. *Buildings* 4(3): 418–436.

Martínez CA, Curadelli O and Compagnoni ME (2013) Optimal design of passive viscous damping systems for buildings under seismic excitation. *Journal of Constructional Steel Research* 90: 253–264.

Ohtori Y, Christenson R, Spencer B Jr, et al. (2004) Benchmark control problems for seismically excited nonlinear buildings. *Journal of Engineering Mechanics* 130(4): 366–385.

Olmati P, Petrini F and Gkoumas K (2014) Fragility analysis for the performance-based design of cladding wall panels subjected to blast load. *Engineering Structures* 78: 112–120.

Pantoli E and Hutchinson T (2015) Experimental and analytical study of the dynamic characteristics of architectural precast concrete cladding. In: Second ATC & SEI conference on improving the seismic performance of existing buildings and other structures, San Francisco, CA, 10–12 December 2015, pp. 560–574.

PEER (2011) Pacific earthquake engineering research center (PEER). PEER ground motion database. Available at: http://ngawest2.berkeley.edu/.

Pinelli J-P, Craig JI and Goodno BJ (1995) Energy-based seismic design of ductile cladding systems. *Journal of Structural Engineering* 121(3): 567–578.

Pipitone G, Barone G and Palmeri A (2018) Optimal design of double-skin façades as vibration absorbers. *Structural Control and Health Monitoring* 25(2): e2086.

Polycarpou PC, Komodromos P and Polycarpou AC (2013) A nonlinear impact model for simulating the use of rubber shock absorbers for mitigating the effects of structural pounding during earthquakes. *Earthquake Engineering & Structural Dynamics* 42(1): 81–100.

Ray-Chaudhuri S and Hutchinson TC (2011) Effect of nonlinearity of frame buildings on peak horizontal floor acceleration. *Journal of Earthquake Engineering* 15(1): 124–142.

Sakr TA (2017) Vibration control of buildings by using partial floor loads as multiple tuned mass dampers. *HBRC Journal* 13(2): 133–144.

Scruggs J and Iwan W (2003) Control of a civil structure using an electric machine with semiactive capability. *Journal of Structural Engineering* 129(7): 951–959.

Simiu E and Scanlan RH (1996) *Wind Effects on Structures: Fundamentals and Application to Design*. Hoboken, NJ: John Willey & Sons Inc, Vol. 605.

Theobald M and Nurick G (2010) Experimental and numerical analysis of tube-core claddings under blast loads. *International Journal of Impact Engineering* 37(3): 333–348.

Tributsch A and Adam C (2012) Evaluation and analytical approximation of tuned mass damper performance in an earthquake environment. *Smart Structures and Systems* 10(2): 155–179.

Van Paepegem W, Palanivelu S, Degrieck J, et al. (2014) Blast performance of a sacrificial cladding with composite tubes for protection of civil engineering structures. *Composites Part B: Engineering* 65: 131–146.

Vanmarcke EH (1975) On the distribution of the first-passage time for normal stationary random processes. *Journal of Applied Mechanic* 42: 215–220.

Vickery PJ, Wadhera D, Galsworthy J, et al. (2009) Ultimate wind load design gust wind speeds in the United States for use in ASCE-7. *Journal of Structural Engineering* 136(5): 613–625.

Wang Y, Liew JR, Lee SC, et al. (2017) Crushing of a novel energy absorption connector with curved plate and aluminum foam as energy absorber. *Thin-Walled Structures* 111: 145–154.

Wu C and Sheikh H (2013) A finite element modelling to investigate the mitigation of blast effects on reinforced concrete panel using foam cladding. *International Journal of Impact Engineering* 55: 24–33.

Xiang P and Nishitani A (2014) Seismic vibration control of building structures with multiple tuned mass damper floors integrated. *Earthquake Engineering & Structural Dynamics* 43(6): 909–925.

Xiang P and Nishitani A (2015) Optimum design of tuned mass damper floor system integrated into bending-shear type building based on h∞, h2, and stability maximization criteria. *Structural Control and Health Monitoring* 22(6): 919–938.

Yang Y, Fallah A, Saunders M, et al. (2011) On the dynamic response of sandwich panels with different core set-ups subject to global and local blast loads. *Engineering Structures* 33(10): 2781–2793.